Antiviral function and viral antagonism of the rapidly evolving dynein activating adapter NINL

Authors

Donté Alexander Stevens[1,*], Christopher Beierschmitt[2,*], Swetha Mahesula[1,3], Miles R. Corley[2], John Salogiannis[1,4], Brian V. Tsu[2], Bryant Cao[2], Andrew P. Ryan[2], Samara L. Reck-Peterson[1,3,5,‡], and Matthew D. Daugherty[2,‡]

[1]Department of Cellular and Molecular Medicine, University of California, San Diego; San Diego, CA, United States

[2]Department of Molecular Biology, University of California, San Diego; San Diego, CA, United States

[3]Howard Hughes Medical Institute; Chevy Chase, MD, United States

[4]Current address, Department of Molecular Physiology and Biophysics, University of Vermont, Burlington VT, United States

[5]Department of Cell and Developmental Biology, University of California, San Diego; San Diego, CA, United States

* These authors contributed equally

‡ Co-corresponding authors: Matthew D. Daugherty (mddaugherty@ucsd.edu) and Samara L. Reck-Peterson (sreckpeterson@health.ucsd.edu)

Abstract

Viruses interact with the intracellular transport machinery to promote viral replication. Such host-virus interactions can drive host gene adaptation, leaving signatures of pathogen-driven evolution in host genomes. Here we leverage these genetic signatures to identify the dynein activating adaptor, ninein-like (NINL), as a critical component in the antiviral innate immune response and as a target of viral antagonism. Unique among genes encoding components of active dynein complexes, NINL has evolved under recurrent positive (diversifying) selection, particularly in its carboxy-terminal cargo binding region. Consistent with a role for NINL in host immunity, we demonstrate that NINL knockout cells exhibit an impaired response to interferon, resulting in increased permissiveness to viral replication. Moreover, we show that proteases encoded by diverse picornaviruses and coronaviruses cleave and disrupt NINL function in a host- and virus-specific manner. Our work reveals the importance of NINL in the antiviral response and the utility of using signatures of host-virus conflicts to uncover new components of antiviral immunity and targets of viral antagonism.

Introduction

Viruses interact directly with host proteins at nearly every step of their replication cycle. Such molecular interactions can either benefit the host (*e.g.,* immune recognition) or the virus (*e.g.,* viral co-option of host machinery or viral antagonism of host immunity) and are thus critical determinants of the outcome of a viral infection. Competing genetic innovations on both sides of these host-virus conflicts result in signatures of recurrent adaptation that have been described as molecular ‘arms races’ (Daugherty and Malik, 2012; Duggal and Emerman, 2012; Tenthorey et al., 2022). Indeed, many host antiviral factors that directly interact with viral proteins display signatures of recurrent positive (diversifying) selection over evolutionary time, and genetic

variation in these host-virus interactions shapes species-specific susceptibility to circulating and emerging pathogens (Daugherty and Malik, 2012; Duggal and Emerman, 2012; Tenthorey et al., 2022; Meyerson and Sawyer, 2011; Rothenburg and Brennan, 2020). These data suggest that there is great potential to use evolutionary signatures of rapid evolution not only as an approach to more deeply understand known host-virus conflicts but also as a means to discover new proteins engaged in viral interactions (Daugherty and Malik, 2012). Compellingly, it is estimated that around 30% of all adaptive amino acid changes in humans result from viral selective pressure (Enard et al., 2016; Enard and Petrov, 2018), suggesting that many host-virus conflicts remain undescribed.

One potential source of host-virus conflicts is over the active transport of macromolecules within the cell. The relatively large size of eukaryotic cells, coupled with the density of macromolecules in the cytoplasm, limits the effectiveness of diffusion to localize and transport large intracellular components, such as organelles, membrane vesicles, RNAs, and protein complexes (Luby-Phelps, 2000; Seksek et al., 1997). Eukaryotic cells overcome this problem by actively transporting large intracellular cargos using dynein and kinesin motors, which move on microtubules in opposite directions. Aspects of viral infection, viral replication, and the host immune response all require microtubule-based transport. For example, viruses co-opt the microtubule cytoskeleton for cell entry, transport of viral components to sites of replication, remodeling of cellular compartments, and viral egress (Brandenburg and Zhuang, 2007; Dodding and Way, 2011; Döhner et al., 2005; Radtke et al., 2006). Similarly, in response to infection, the host adaptive and innate immune response require movement of signaling components, transport of endocytic and exocytic vesicles, organelle recycling, and cellular remodeling, all of which require the microtubule-based trafficking machinery (Ilan-Ber and Ilan, 2019; Kast and Dominguez, 2017; Man and Kanneganti, 2016; Mostowy and Shenoy, 2015). Despite the clear

role of microtubule-based transport in both aiding and inhibiting viral replication, the degree to which host-virus conflicts shape the basic biology of this machinery is poorly understood.

To uncover the role of this machinery in viral replication and the immune response, we set out to determine if there were undescribed genetic conflicts between viruses and the intracellular transport machinery. Specifically, we focused on the dynein transport machinery, which traffics dozens of cellular cargos towards microtubule minus-ends (generally anchored to centrosomes near the nucleus). In human cells, only one dynein motor-containing gene, cytoplasmic dynein-1 (*DYNC1H1*), is responsible for long-distance transport in the cytoplasm. However, the active cytoplasmic dynein-1 complex (dynein hereafter) is composed of multiple dynein subunits, the multisubunit dynactin complex, and one of a growing list of activating adaptors (McKenney et al., 2014; Schlager et al., 2014). Interestingly, it is the activating adaptors that provide cargo specificity for dynein in addition to their essential role in activating robust processive motility (Olenick and Holzbaur, 2019; Reck-Peterson et al., 2018). However, the specific biological functions of most activating adaptors remain unknown.

We now show that one activating adaptor, ninein-like protein (NINL, also known as NLP), has evolved under recurrent positive selection in primates, making it unique among all analyzed dynein, dynactin, and activating adaptor genes. Based on the hypothesis that such an evolutionary signature in NINL could be the result of a previously undescribed host-virus conflict, we explored the function of NINL in the antiviral immune response. Using NINL knockout (KO) cells, we find that NINL is important for limiting viral infection, especially in the presence of the antiviral signaling cytokine, type I interferon (IFN). We further demonstrate that this attenuation of the antiviral efficacy of IFN in NINL KO cells is due to a dramatic decrease in interferon-stimulated gene (ISG) production. Finally, we show that diverse proteases from picornaviruses and coronaviruses cleave NINL at several host-specific sites, resulting in a disruption of NINL's ability

to traffic cargo. Together, our results reveal a novel immune function for NINL as well as a means by which viruses may antagonize NINL function in a virus- and host-specific manner. More broadly, our work implicates a component of the dynein transport machinery as a rapidly evolving barrier to viral replication, and highlights the utility of an evolution-guided approach for discovery of new host-virus conflicts.

Results

The dynein activating adaptor, NINL, has evolved under positive selection

Active dynein complexes in human cells are large, multi-subunit machines. The dynein/dynactin complex is composed of two copies of the ATPase-containing heavy chain, two copies of five additional dynein chains, the 23-subunit dynactin complex, and an activating adaptor (Olenick and Holzbaur, 2019; Reck-Peterson et al., 2018) (Figure 1A). To generate hypotheses about potential conflicts between the dynein machinery and pathogens, we searched for signatures of positive selection during primate evolution in genes for all dynein/dynactin subunits and the 13 activating adaptors known at the time of this analysis. Each human dynein gene was compared to orthologs in 13-20 diverse simian primates, and a gene-wide dN/dS (also known as omega) value was calculated, which compares the gene-wide rate of nonsynonymous changes (*i.e.*, amino acid altering) to the rate of synonymous (*i.e.*, silent) changes. Consistent with the critical role of dynein-mediated intracellular transport, most genes we analyzed were extremely well conserved with dN/dS values of <0.1, while one dynein activating adaptor, NINL, showed an elevated rate compared to the rest (Figure 1B and Supplementary File 1). To determine whether any genes had individual codons that have been subject to recurrent positive selection, we performed codon-based analyses of positive selection. Consistent with their low dN/dS values, we observed that most dynein, dynactin and activating adaptor genes showed no evidence for positive selection (p-value > 0.05). In contrast, NINL showed strong evidence for recurrent positive

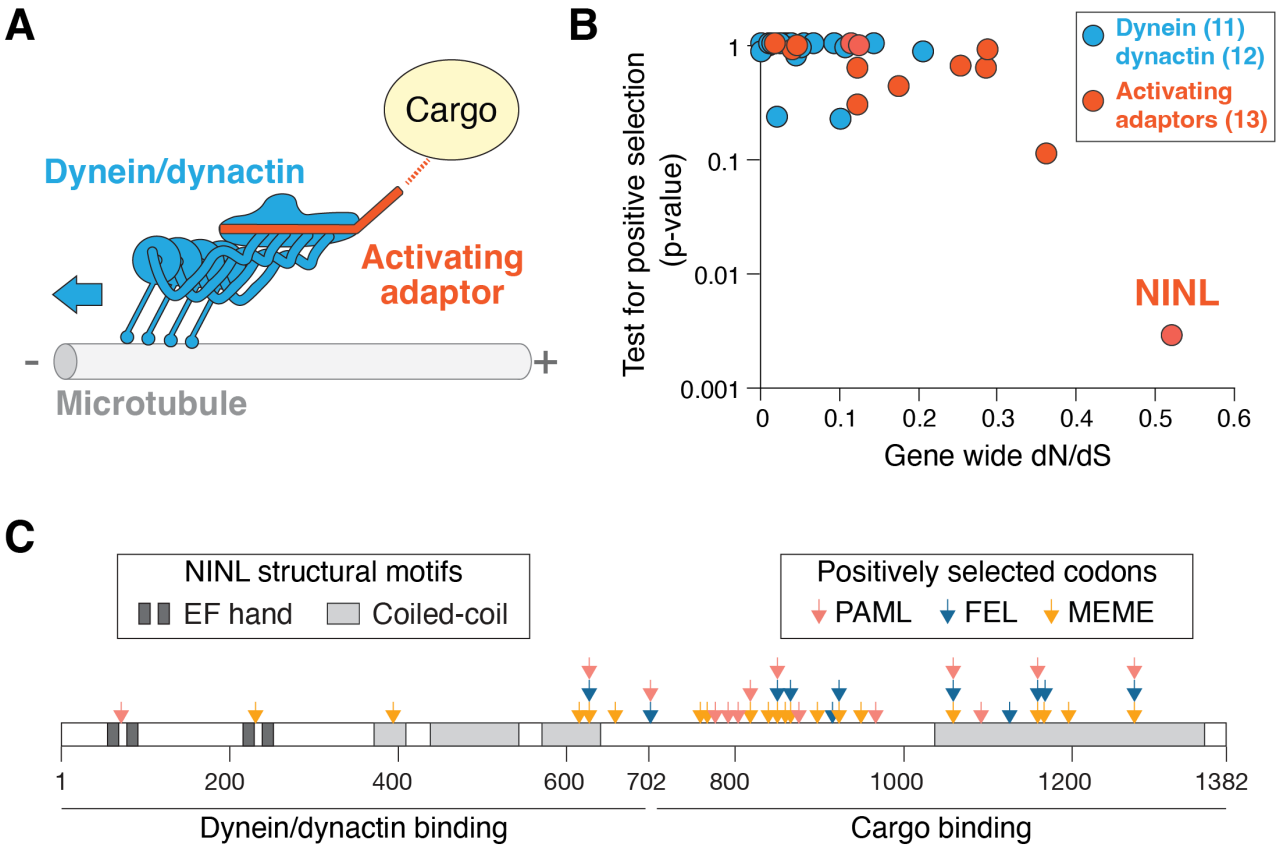

D

	dN/dS	p-value
Full length	0.52	0.003
N-terminus Dynein/dynactin binding	0.31	>0.5
C-terminus Cargo binding	0.74	0.0004

Figure 1. The dynein activating adaptor, NINL, has evolved under positive selection in primates. (**A**) A schematic of the cytoplasmic dynein-1 transport machinery, which includes dynein and dynactin subunits (blue) and an activating adaptor (orange). Dynein moves toward the minus end of microtubules (blue arrow). (**B**) A scatterplot displaying evolutionary signatures of selection for 23 dynein and dynactin genes (blue) and 13 dynein activating adaptor genes (orange). The x-axis displays the rate of non-synonymous changes (dN) divided by the rate of synonymous changes (dS) in the coding sequence across primate evolution. The y-axis displays the calculated probability of the gene having evolved under positive selection using PAML. Complete data are found in Figure 1–figure supplement 1. (**C**) A schematic of human NINL isoform 1 with EF hand (dark grey) and coiled-coil (light grey) domains shown. The amino-terminal dynein/dynactin binding region and the carboxy-terminal candidate cargo binding domains are indicated. Sites of positive selection predicted by three evolutionary models are shown as colored arrows: PAML (light red), FEL (blue), MEME (orange). A full list of sites and their calculated probabilities are shown in Figure 1–figure supplement 2. (**D**) Full-length NINL, the dynein/dynactin binding amino-terminus of NINL and the candidate cargo binding carboxy-terminus of NINL were analyzed for signatures of positive selection. Select dN/dS and p-values are shown, with additional evolutionary data in Figure 1–figure supplement 3.

(Line-numbered figure legends are also found at the end of the document).

selection in primates, consistent with previous data (Gordon et al., 2020) (Figure 1B and Supplementary File 1), establishing the possibility that NINL could be at the interface of a host-pathogen interaction.

In order to attribute the signatures of positive selection in NINL to known functional domains within NINL, we performed additional analyses to identify specific codons that have evolved under positive selection using three independent methods, PAML, FEL, and MEME (Kosakovsky Pond and Frost, 2005; Murrell et al., 2012; Yang, 2007). We identified 30 codons that show signatures of positive selection based on one or more of these methods (Figure 1C and Supplementary File 2). Most (24 of 30) of these codons are excluded from the known dynein/dynactin binding region of NINL (residues 1-702) (Redwine et al., 2017) and instead are located in the carboxy-terminal region of the protein that is expected to interact with cargo (residues 703-1382). When we analyzed individual domains on their own, we found no evidence for positive selection in the amino-terminus alone, while the carboxy-terminus retained a significant signature of positive selection (Figure 1D and Supplementary File 3). Taken together, our evolutionary analyses indicate that NINL stands out among components of the active dynein complex by having evolved under recurrent positive selection in primates.

Viral replication is increased in cells lacking NINL

Our observation that NINL displays a signature of positive selection that is unique among dynein components led us to hypothesize that NINL may be co-opted by viruses for viral replication or may play a role in the immune response to viruses. To evaluate this hypothesis, we generated a human A549 cell line that lacked NINL (NINL KO) (Figure 2A, Figure 2–figure supplement 1A, B). At a qualitative level, these cells appeared to have a normal microtubule architecture and centrosomes (Figure 2–figure supplement 1A). In parallel, we generated cells that lacked ninein (NIN KO) (Figure 2A, Figure 2–figure supplement 1C), the closest human paralog to NINL, which

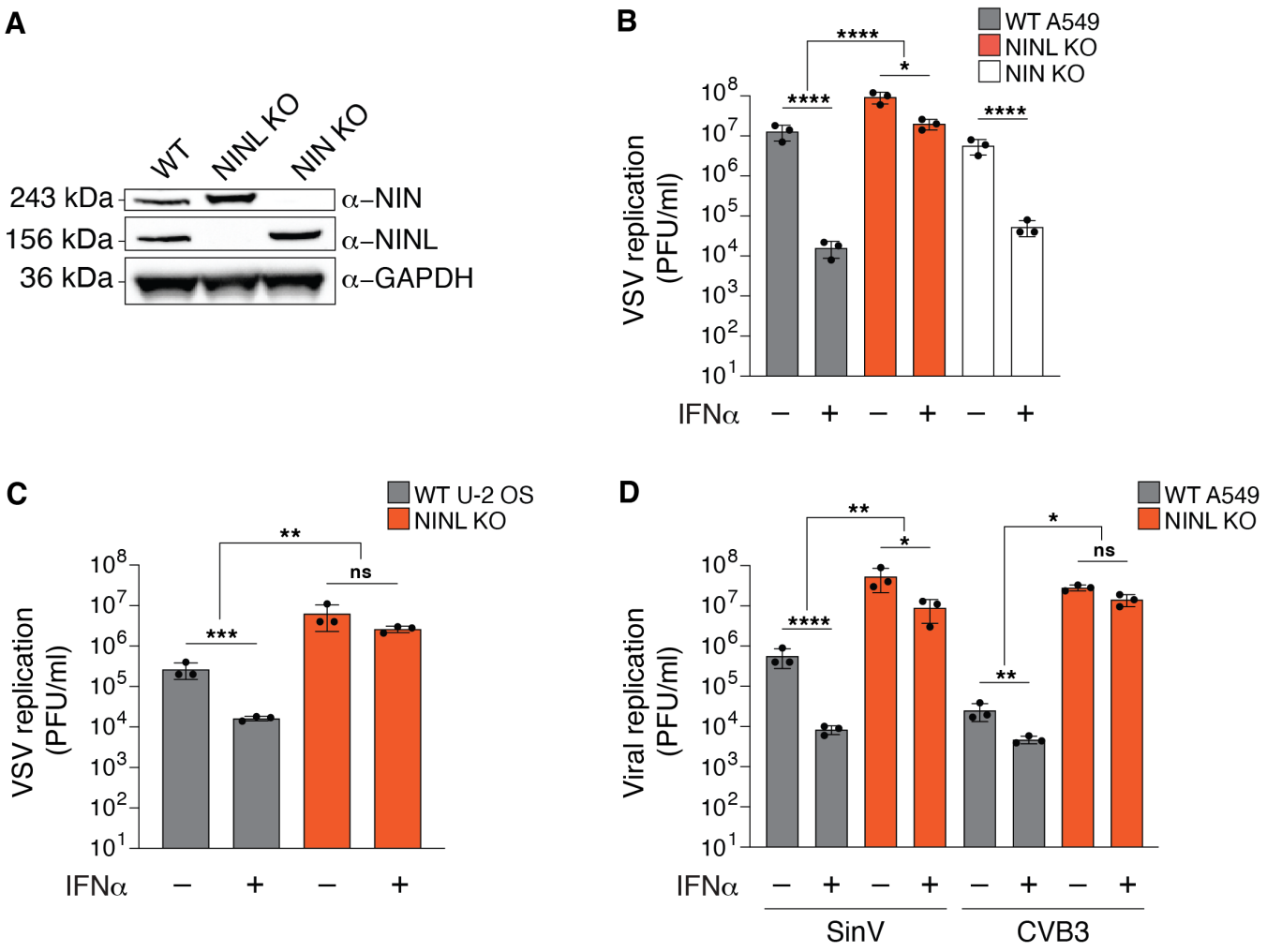

Figure 2. The antiviral potency of IFNα is reduced in NINL KO cells. (**A**) Immunoblots of WT A549 cells, and CRISPR/Cas9-generated NINL and NIN KO A549 cells probed with the indicated antibodies. GAPDH served as a loading control. Protein molecular weight markers are shown in kilodaltons (kDa) to the left of each immunoblot. Representative images from three biological replicates are shown. (**B**) WT, NINL KO, and NIN KO A549 cells were treated with 100U IFNα for 24 hours and then infected with VSV (5000 PFU/mL, MOI ≈ 0.01). Virus-containing supernatants were collected nine hours post-infection and viral titers (y-axis, plaque forming units per mL) were determined by plaque assay. (**C**) WT or NINL KO U-2 OS cells were treated with 100U IFNα for 24 hours and then infected with VSV (5000 PFU/mL, MOI ≈ 0.01). Virus-containing supernatant was collected nine hours post-infection and viral titers (y-axis, plaque forming units per mL) were determined by plaque assay. (**D**) WT or NINL KO A549 cells were treated with 100U IFNα for 24 hours and then infected with Sindbis virus (500,000 PFU/mL, MOI ≈ 1.0) (left) or treated with 1000U IFNα for 24 hours and then infected with coxsackievirus B3 (5000 PFU/mL, MOI ≈ 0.01) (right). Virus-containing supernatants were collected 24 hours post-infection and viral titers (y-axis, plaque forming units per mL) were determined by plaque assay. (**B-D**) Data are presented as mean ± standard deviation of three biological replicates, with individual points shown. Data were analyzed by two-way ANOVA with Tukey's method adjustment for multiple comparisons for IFNα treatment within each cell line, two-way ANOVA interaction comparison for IFNα interaction between cell lines. *p<0.05, **p<0.01, ***p<0.001, ****p<0.0001, ns = not significant.

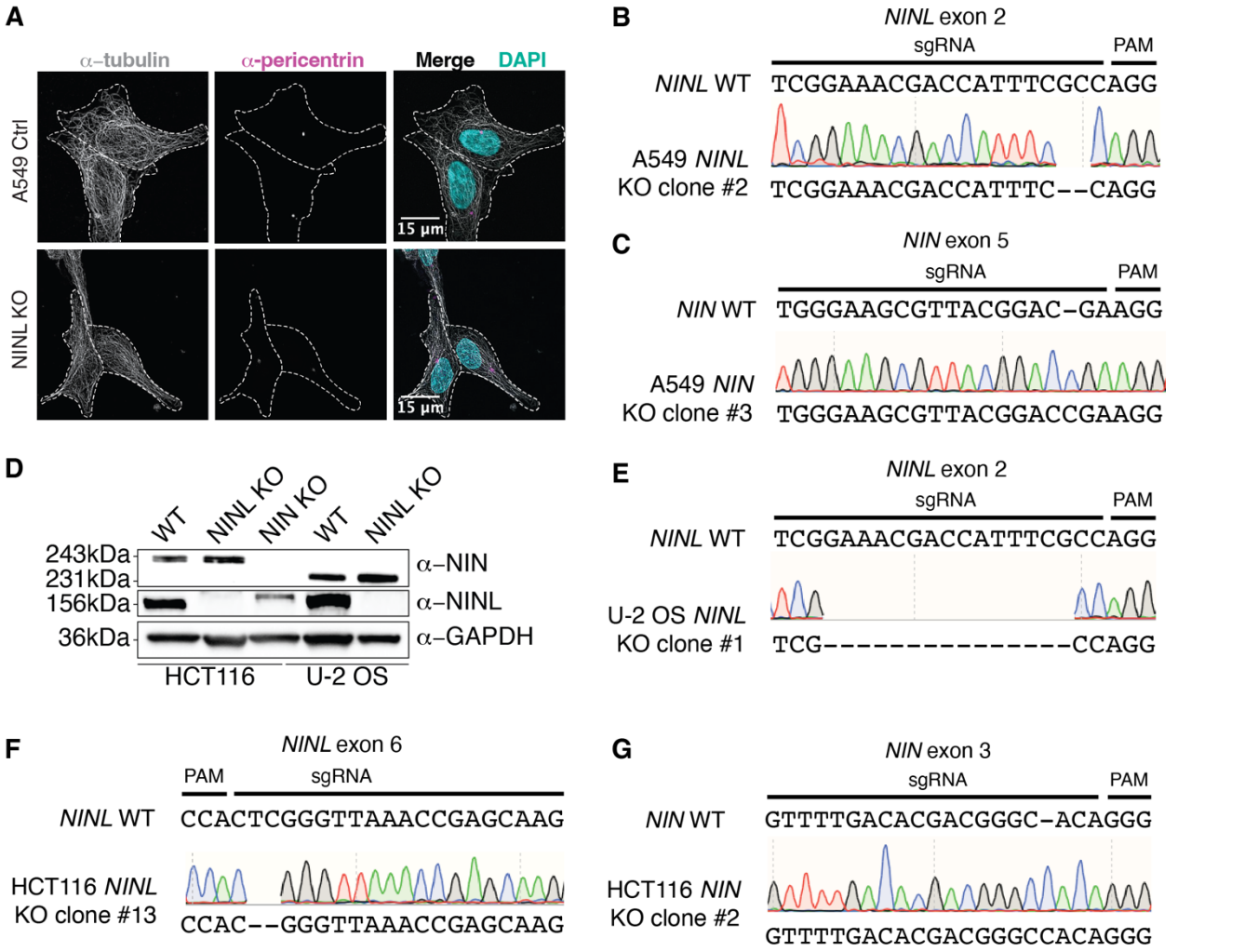

Figure 2–figure supplement 1. Validation of CRISPR/Cas9-editing to generate NINL and NIN KO cells. (**A**) Confocal micrographs displayed as maximum intensity projections of WT and NINL KO A549 cells. Immunostaining with anti-pericentrin and anti-tubulin antibodies was used to visualize centrosomes and microtubules, respectively. Nuclei were visualized with DAPI. 15 μm scale bars are shown in the merged micrographs. Dashed white lines denote cellular boundaries. Representative micrographs from two biological replicates are shown. (**B**) Sequence verification of exon 2-targeted NINL KO A549 cells. An excerpt of the WT *NINL* sequence is shown with the CRISPR-targeting sgRNA and PAM sequences indicated (top), the sequencing chromatogram (middle), and the sequence of the NINL KO (bottom). (**C**) Sequence verification of exon 5-targeted NIN KO A549 cells. (**D**) Immunoblots of control (CTRL) HCT116 and U-2 OS cells, and CRISPR/Cas9-generated NINL and NIN KO HCT116 and U-2 OS cells probed with the indicated antibodies. GAPDH served as a loading control. Protein molecular weight markers are shown in kilodaltons (kDa) to the left of each immunoblot. Representative images from three biological replicates are shown. (**E**) Sequence verification of exon 2-targeted NINL KO U-2 OS cells. (**F**) Sequence verification of exon 6-targeted NINL KO HCT116 cells. (**G**) Sequence verification of exon 3-targeted NIN KO HCT116 cells.

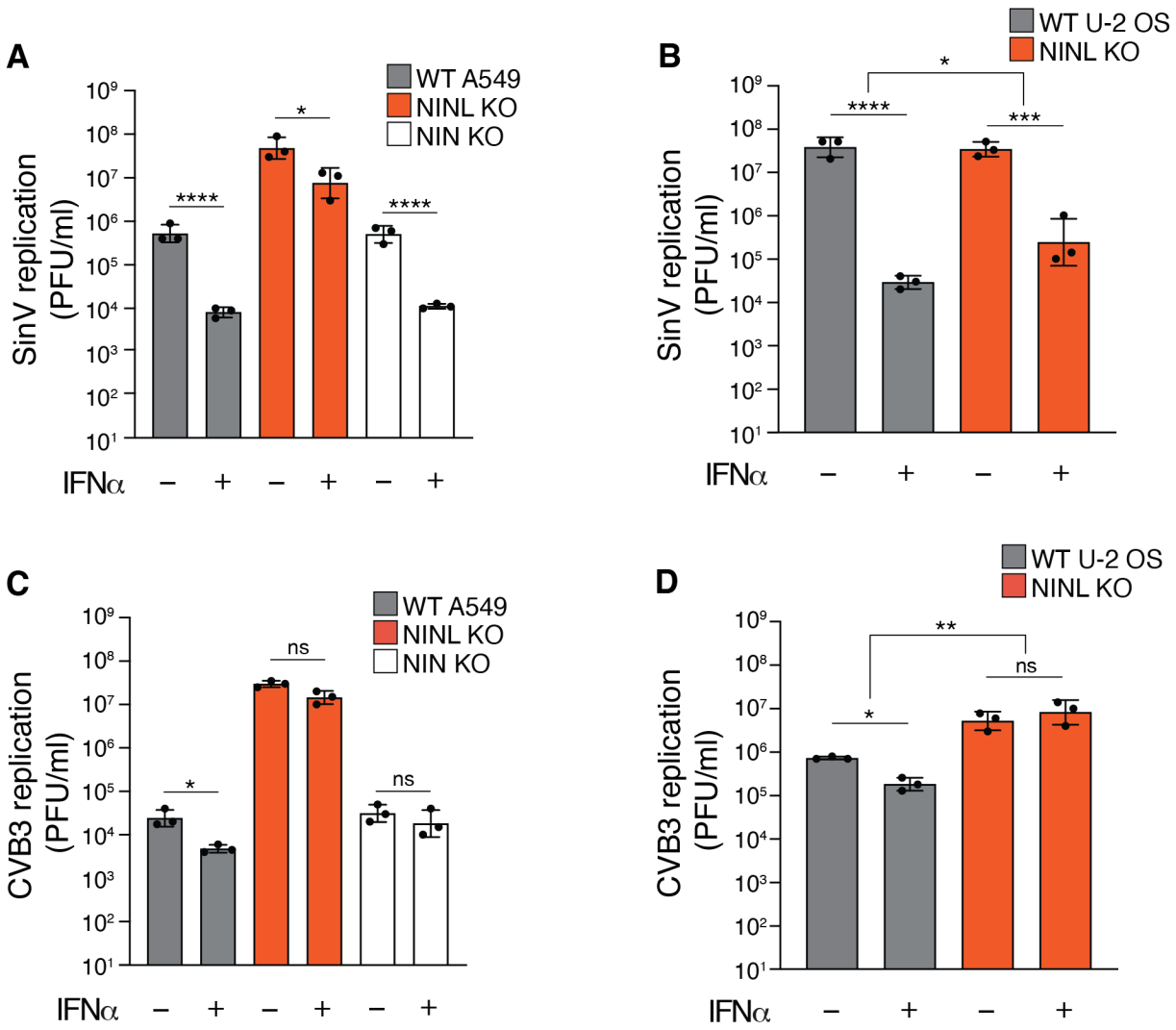

Figure 2–figure supplement 2. Reduction of IFNα-mediated antiviral response is observed across multiple cell lines. (**A**) A549 WT, NINL KO, or NIN KO cells were treated with 100U IFNα for 24 hours, then infected with Sindbis virus (500,000 PFU/mL, MOI ≈ 1.0). Cells were collected 24 hours post-infection and viral titers (y-axis, plaque forming units per mL) were determined by plaque assay. WT and NINL KO data are reproduced from Figure 2D for comparison. (**B**) U-2 OS WT or NINL KO cells were treated, infected, harvested, and quantified as described in **(A).** (**C**) A549 WT, NINL KO, or NIN KO cells were treated with 1000U IFNα for 24 hours, then infected with coxsackievirus B3 (5,000 PFU/mL, MOI ≈ 0.01). Cells were collected 24 hours post-infection and viral titers (y-axis, plaque forming units per mL) were determined by plaque assay. WT and NINL KO data are reproduced from Figure 2D for comparison. (**D**) U-2 OS WT or NINL KO cells treated, infected, harvested, and quantified as described in (C). (A-D) Data are presented as mean ± standard deviation of three biological replicates, with individual points shown. Data were analyzed by two-way ANOVA with Tukey's method adjustment for multiple comparisons for IFNα treatment within each cell line, two-way ANOVA interaction comparison for IFNα interaction between cell lines. *p<0.05, **p<0.01, ***p<0.001, ****p<0.0001, ns = not significant.

shares a similar domain architecture with NINL and is also a dynein activator adaptor (Redwine et al., 2017), but shows no evidence for positive selection (Figure 1B and Supplementary File 1). To evaluate the effect that NINL or NIN have on viral replication or the innate immune response to viral infection, we infected WT, NINL KO, or NIN KO A549 cells with a model enveloped negative-sense single-stranded RNA (-ssRNA) virus, vesicular stomatitis virus (VSV), with and without pretreatment with the antiviral signaling cytokine interferon alpha (IFNα). Consistent with the strong antiviral effect of IFNα, we observed a >100-fold decrease in viral replication in WT and NIN cells that had been pretreated with IFNα (Figure 2B). In contrast, we observed that the effect of IFNα was significantly attenuated in NINL KO cells, where we found that IFNα pretreatment reduced VSV replication <10-fold (Figure 2B). To attribute the changes in viral replication to the absence of NINL rather than off-target perturbations or cell-line specific effects, we generated additional NINL KO cell lines in human U-2 OS cells (Figure 2–figure supplement 1D, E). We again observed that NINL KO cells had a significant reduction in the antiviral effects of IFNα pretreatment (Figure 2C). We also noted that VSV replication was higher in NINL KO cell lines compared to WT even in the absence of IFN, which may indicate either a basal defect in the antiviral response in NINL KO cells or a second function of NINL that is IFN independent. To test whether the NINL-dependent effect on IFN antiviral potency was specific to VSV replication, we tested two positive-sense single-stranded RNA (+ssRNA) viruses: Sindbis virus (SinV)– an enveloped virus, and coxsackievirus B3 (CVB3)– a non-enveloped virus in both A549 and U-2 OS cells. In both cases, we observed a potent antiviral effect of IFNα pretreatment in WT and NIN KO cells, while this effect was reduced in NINL KO cells (Figure 2D, Figure 2–figure supplement 2A-D). The attenuation of the IFN-induced antiviral effect against viruses from three distinct families suggests that NINL may broadly play a role in the IFN-mediated innate immune response to viruses.

178 **Loss of NINL results in an attenuated antiviral immune response**

179 Based on the reduced antiviral potency of IFNα in cells lacking NINL, we next investigated
180 whether there was an attenuation of IFN-mediated signaling in NINL KO cells. Type I IFNs, such
181 as IFNα, activate the Janus kinase/signal transducer and activator of transcription (JAK/STAT)
182 pathway to trigger the expression of IFN-stimulated genes (ISGs), which include potent antiviral
183 effectors (Schoggins, 2019). Therefore, we asked whether there was a defect in the JAK/STAT
184 signaling cascade by western blot analysis of the phosphorylation of the transcription factors
185 STAT1 (pSTAT1(Y701)) and STAT2 (pSTAT2(Y690)) as well as the induction of ISG expression
186 following IFNα pretreatment. Despite robust phosphorylation of STAT1 and STAT2 in response
187 to IFNα pretreatment in WT, NINL KO, and NIN KO cells, protein expression of the canonical
188 ISGs–MX1, IFIT3, OAS1, and ISG15 was greatly reduced in NINL KO cells relative to WT or NIN
189 KO cells (Figure 3A). To again confirm that this was not specific to cell type, we showed that this
190 lack of ISG protein expression was independent of cell background or the choice of CRISPR guide
191 (Figure 2–figure supplement 1A-G, Figure 3–figure supplement 1). Next, we performed RNAseq
192 analyses on WT, NINL KO, and NIN KO A549 cells in the presence or absence of IFNα
193 pretreatment (Supplementary File 4). In WT cells, we identified 88 ISGs that were significantly
194 (adjusted p-value ≤ 0.05, log2fold change ≥ 1) upregulated in response to IFN treatment (Figure
195 3–figure supplement 2). We then compared the transcriptional profiles of these ISGs between
196 IFNα-treated WT, NINL KO, and NIN KO cells. Consistent with our western blot analysis, the
197 induction pattern of ISG transcripts in WT and NIN KO cells was similar, whereas many ISG
198 transcripts from IFNα treated NINL KO cells were downregulated compared to IFNα treated WT
199 cells (Figure 3B, Figure 3–figure supplement 3 and Figure 3–figure supplement 4). Other
200 transcripts unrelated to the IFN response also showed altered expression in NINL KO cells
201 relative to WT cells (Figure 3–figure supplement 4 and Supplementary File 4). However, the
202 overall lower expression of ISGs in NINL KO relative to WT cells (Figure 3-figure supplement 4)
203

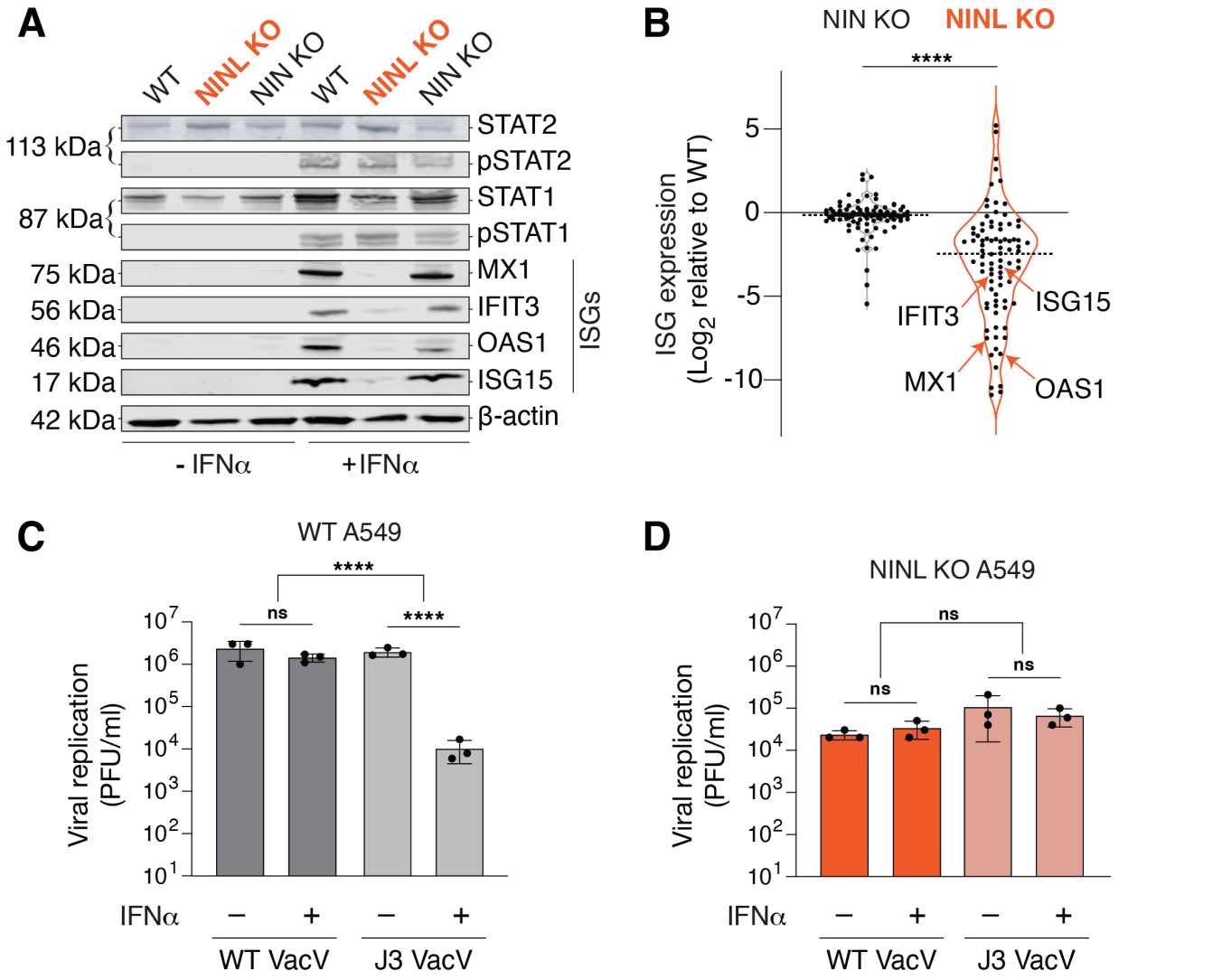

Figure 3. NINL KO cells fail to mount an effective IFN response. (**A**) Immunoblot of extracts from WT, NINL KO, and NIN KO A549 cells untreated (-) or treated (+) with IFNα. Immunoblots were probed with anti-STAT2, anti-Phospho-STAT2 (Tyr690), anti-STAT1, anti-Phospho-STAT1 (Tyr701), anti-Mx1, anti-IFIT3, anti-OAS1, anti-ISG15, and anti-β-actin antibodies. Predicted protein molecular weights are shown in kilodaltons (kDa) to the left of each immunoblot. Representative images from three biological replicates are shown. (**B**) Differential ISG expression in WT, NINL KO, and NIN KO cells induced with IFNα. ISGs were identified as the 88 genes whose expression was upregulated in WT cells after IFNα pretreatment (Figure 3-figure supplement 2). Experiments were performed with three biological replicates. Data are displayed as a violin plot of ISG expression in NIN KO or NINL KO cells relative to WT cells. **** = p<0.0001 based on paired t-test. Dotted line indicates mean. Individual data points for ISGs shown in panel (A) are indicated. (**C**) A549 WT cells were treated with 1000U IFNα for 24 hours, then infected with wild-type vaccinia virus (WT VacV) or J3 mutant vaccinia virus (J3 VacV) (50,000 PFU/mL, MOI ≈ 0.1). Cell-associated virus was collected 24 hours post-infection and viral titers (y-axis, plaque forming units per mL) were determined by plaque assay. (**D**) A549 NINL KO cells were treated, infected, harvested, and quantified as described in (C). (C-D) Data are presented as mean ± standard deviation of three biological replicates, with individual points shown. Data were analyzed by two-way ANOVA with Tukey's method adjustment for multiple comparisons for IFNα treatment within each cell line, two-way ANOVA interaction comparison for IFNα interaction between cell lines. ****p<0.0001, ns = not significant.

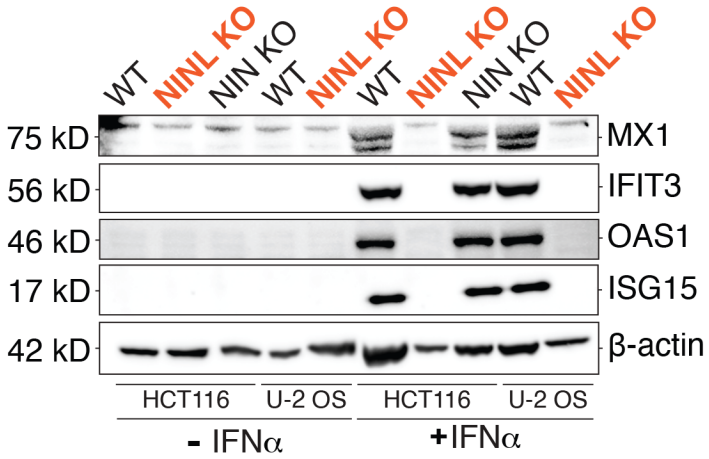

Figure 3–figure supplement 1. Reduced ISG production occurs following NINL KO in multiple cell lines generated using different CRISPR gRNAs Immunoblot of extracts from WT, NINL KO, NIN KO HCT116 cells and WT and NINL KO U-2 OS cells untreated or treated with IFNα. Immunoblots were probed with anti-STAT2, anti-Phospho-STAT2 (Tyr690), anti-STAT1, anti-Phospho-STAT1 (Tyr701), anti-Mx1, anti-IFIT3, anti-OAS1, anti-ISG15, and anti-β-actin antibodies. Predicted protein molecular weights are shown in kilodaltons (kDa) to the left of each immunoblot. Representative images from three biological replicates are shown.

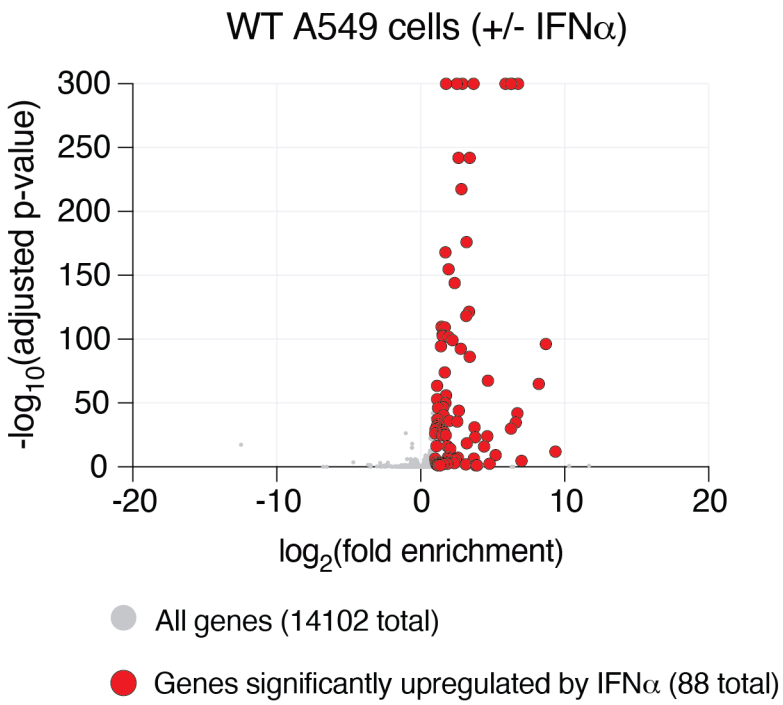

Figure 3–figure supplement 2. Identification of 88 ISGs in WT A549 cells. Differential gene expression from RNAseq analyses of WT A549 cells pretreated with IFNα compared to untreated. Each condition (untreated or IFNα) was performed with three biological replicates, with independent RNA extractions, sequencing library preparation, and sequencing. RNA levels for a total of 14102 genes (grey dots) could be compared (see Materials and Methods and Supplementary File 4). Only 88 genes (red dots) showed a statistically significant upregulation (adjusted p-value ≤ 0.05, $\log_2$-fold change ≥ 1), which we refer to in subsequent analyses as ISGs.

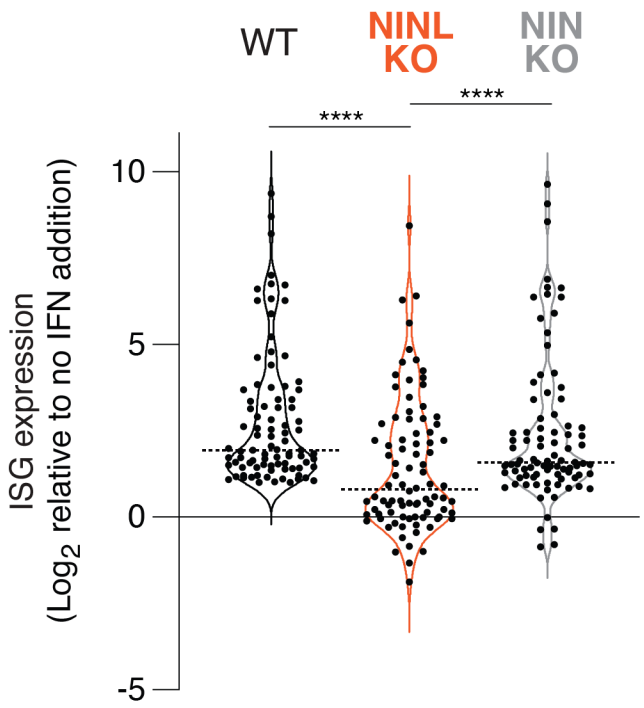

Figure 3–figure supplement 3. Interferon induction has a reduced effect on ISG expression in NINL KO cells. Differential gene expression of 88 ISGs (identified in Figure 3–figure supplement 2**)** from RNAseq analyses of the indicated cell lines pretreated with IFNα compared to untreated. Each condition (untreated or IFNα) was performed with three biological replicates, with independent RNA extractions, sequencing library preparation, and sequencing. Only the 88 genes significantly upregulated in WT cells, which we refer to as ISGs (adjusted p-value ≤0.05, log_2-fold change ≥1), are shown for each cell line. Data are displayed as a violin plot of ISG upregulation, with the dotted line indicating the mean. ****p<0.0001 based on one-way ANOVA test.

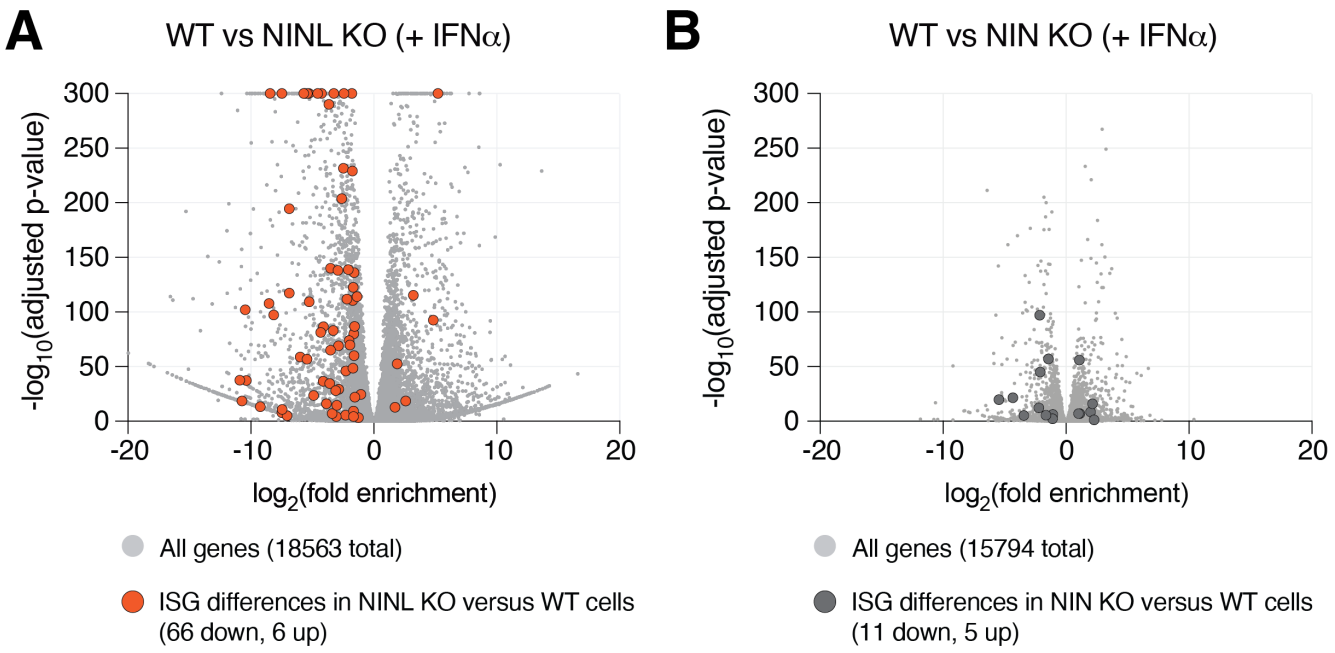

C

Reactome pathway enrichment

Genes with reduced expression in NINL KO cells (+IFNα) compared to WT cells (+IFNα)

Reactome pathway ID	Reactome pathway name	# entities found	# entities total	Entities ratio	Entities p-value	Entities FDR
R-HSA-909733	Interferon alpha/beta signaling	84	190	0.013	1.7 E-05	0.023
R-HSA-3000171	Non-integrin membrane-ECM interactions	36	61	0.0040	2.1 E-05	0.023

Figure 3–figure supplement 4. Differential gene expression in NINL KO and NIN KO cells compared to WT cells. (**A**) Differential gene expression from RNAseq analyses of NINL KO cells treated with IFNα compared to WT A549 cells treated with IFNα. Each cell line (NINL KO or WT) was treated with IFNα with three biological replicates, with independent RNA extractions, sequencing library preparation, and sequencing. RNA levels for a total of 18563 genes (grey dots) could be compared (see Materials and Methods and Supplementary File 4). Orange dots highlight the 72 ISGs that are significantly differentially expressed between cell lines, with the majority (66 of 72) of ISGs significantly lower in NINL KO cells (adjusted p-value ≤0.05, log_2-fold change ≤-1). (**B**) Differential gene expression from RNAseq analyses of NIN KO cells treated with IFNα compared to WT A549 cells treated with IFNα. RNA levels for a total of 15794 genes (grey dots) could be compared (see Materials and Methods and Supplementary File 4). Dark grey dots highlight the 11 ISGs that are significantly differentially expressed between cell lines. (**C**) Reactome pathway analysis (Jassal et al., 2020) of the 3549 genes with significantly lower expression (adjusted p-value ≤0.05, log_2-fold change ≤-1) in NINL KO cells treated with IFNα relative to WT cells treated with IFNα. Only the two pathways shown were identified as significantly different between the cell lines. The number of genes found to be lower in NINL KO cells (# entities found) compared to the number of genes in the indicated pathway (# entities total) is shown. The p-value, as well as false discovery rate (FDR) adjusted p-values are shown.

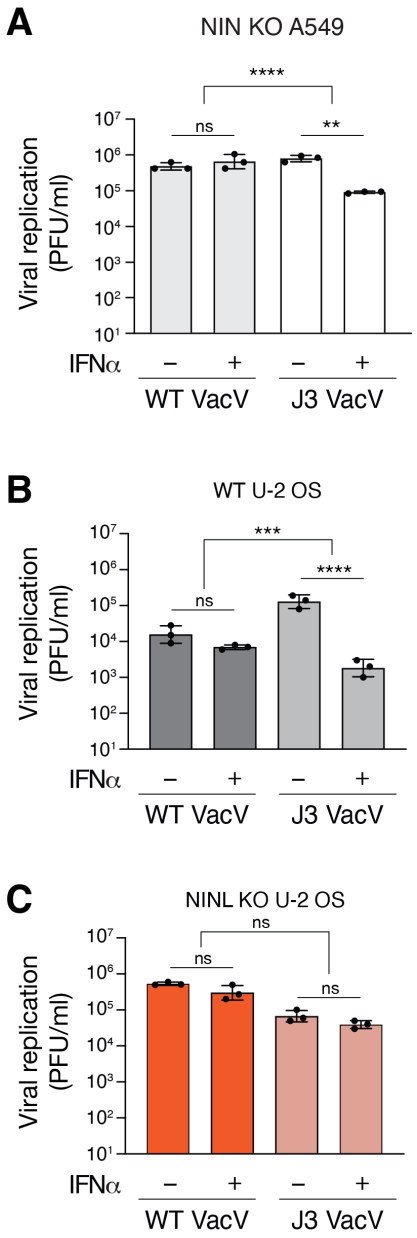

Figure 3–figure supplement 5. NINL KO results in loss of interferon sensitivity of the VacV J3 mutant.

(**A**) A549 NIN KO cells were treated with 1000U IFNα for 24 hours, then infected with wildtype vaccinia virus (VacV WT) or J3 mutant vaccinia virus (J3 VacV) (50,000 PFU/mL, MOI ≈ 0.1). Cell-associated virus was collected 24 hours post-infection and viral titers (y-axis, plaque forming units per mL) were determined by plaque assay. (**B**) U-2 OS WT cells were treated with 1000U IFNα for 24 hours, then infected with wild-type vaccinia virus or J3 mutant vaccinia virus (50,000 PFU/mL, MOI ≈ 0.1). Cells were collected 24 hours post-infection and viral titers (y-axis, plaque forming units per mL) were determined by plaque assay. (**C**) U-2 OS NINL KO cells were treated, infected, harvested, and collected as indicated in (B). (A-C) Data are presented as mean ± standard deviation of three biological replicates, with individual points shown. Data were analyzed by two-way ANOVA with Tukey's method adjustment for multiple comparisons for IFNα treatment within each viral infection, two-way ANOVA interaction comparison for IFNα interaction between viral infections. **p<0.01, *** p<0.001, ns = not significant.

indicates that cells lacking NINL have a distinct defect in their ability to mount an effective antiviral immune response.

To further demonstrate that the lack of ISG expression in cells lacking NINL has a profound effect on the interferon-mediated antiviral response, we took advantage of a virus in which interferon sensitivity can be modulated genetically. Vaccinia virus (VacV) is a large double-stranded DNA virus that is relatively insensitive to the effects of IFNα due to the large number of proteins the virus encodes that antagonize the immune response (Yu et al., 2021). However, a point mutation in the J3 methyltransferase protein (VacV J3) confers interferon sensitivity by sensitizing the virus to the antiviral effects of the IFIT family of ISGs (Daffis et al., 2010; Daugherty et al., 2016; Johnson et al., 2018; Latner et al., 2002). As IFIT1, IFIT2, and IFIT3 were among the ISGs we saw decreased in NINL KO cells relative to WT and NIN KO cells (Supplementary File 4), we hypothesized that NINL KO cells may lack the ability to inhibit the J3 mutant vaccinia virus after IFNα pretreatment. As expected, in WT and NIN KO A549 cells, wildtype VacV (VacV WT) was insensitive to IFNα, whereas VacV J3 replication was significantly reduced upon IFNα pretreatment (Figure 3C, Figure 3–figure supplement 5A). In contrast, mutant and wildtype viruses replicated equivalently in the NINL KO cells regardless of IFNα pretreatment (Figure 3D). We found the same differential response to the J3 VacV mutant between WT and NINL KO cells in U-2 OS cells, showing that this phenotype is not cell type specific (Figure 3–figure supplement 5). All together, these data suggest NINL plays a critical role during the IFN-mediated antiviral immune response, further substantiating our hypothesis that NINL is at the center of an antagonistic host-pathogen interaction.

Viral proteases cleave NINL in a host-specific manner

The IFN response is the first line of host antiviral defense during viral infection. Thus, viruses have developed many strategies to evade or subvert the host IFN response (Beachboard and Horner,

2016; Hoffmann et al., 2015). Our data indicating that NINL is important for the IFN response, combined with the observation that NINL is evolving under positive selection, led us to hypothesize that viruses may antagonize NINL function. One such viral antagonism strategy is to deploy virus-encoded proteases to cleave components of the host antiviral defense system (Lei and Hilgenfeld, 2017; Tsu et al., 2021b). Thus, we next investigated whether viral proteases cleave NINL. Using a predictive model of enteroviral 3C protease ($3C^{pro}$) target specificity (Tsu et al., 2021a), we identified three high-confidence sites of potential cleavage within NINL at residues 231, 827, and 1032 (Figure 4A) in which amino acid diversity within primates is expected to alter $3C^{pro}$ cleavage susceptibility (Figure 4B). Indeed, upon transfection of cells with NINL and CVB3 $3C^{pro}$, we observed an overall reduction of full-length NINL and the appearance of two cleavage products at sizes that correspond to predicted cleavage at sites 827 and 1032 (Figure 4C, D). We also observed a weaker product at a size that corresponds to the predicted size of NINL after cleavage at site 231. To confirm cleavage site specificity, we generated NINL point mutants that take advantage of the diversity of these sites found in primates (Figure 4B). Specifically, we replaced the glutamine immediately preceding the site of cleavage (the P1 position) with an arginine found in non-human primates that we predicted would prevent cleavage by $3C^{pros}$ (Tsu et al., 2021a) for each of the predicted sites. Co-transfection of CVB3 $3C^{pro}$ with NINL containing these mutations individually (Q1032R) or in combination (double mutant Q827R/Q1032R (Double) and triple mutant Q231R/Q827R/Q1032R (Triple)) confirmed the sites of cleavage, with the NINL triple mutant eliminating all cleavage products by CVB3 $3C^{pro}$ (Figure 4D). We also noted that two of these sites (Q827 and Q1032), along with many of the codons predicted to be evolving under positive selection (Figure 1C), reside in a single exon (exon 17) within the carboxy-terminal region of NINL (Figure 4A). Intriguingly, this exon is lacking in an alternatively spliced isoform of NINL (isoform 2) (Dona et al., 2015; Kersten et al., 2012; van Wijk et al., 2009). We, therefore, tested whether isoform 2 is cleaved by CVB3 $3C^{pro}$. Consistent with the loss of two primary sites of cleavage, we observed minimal decrease in the full-length product when isoform 2 was co-

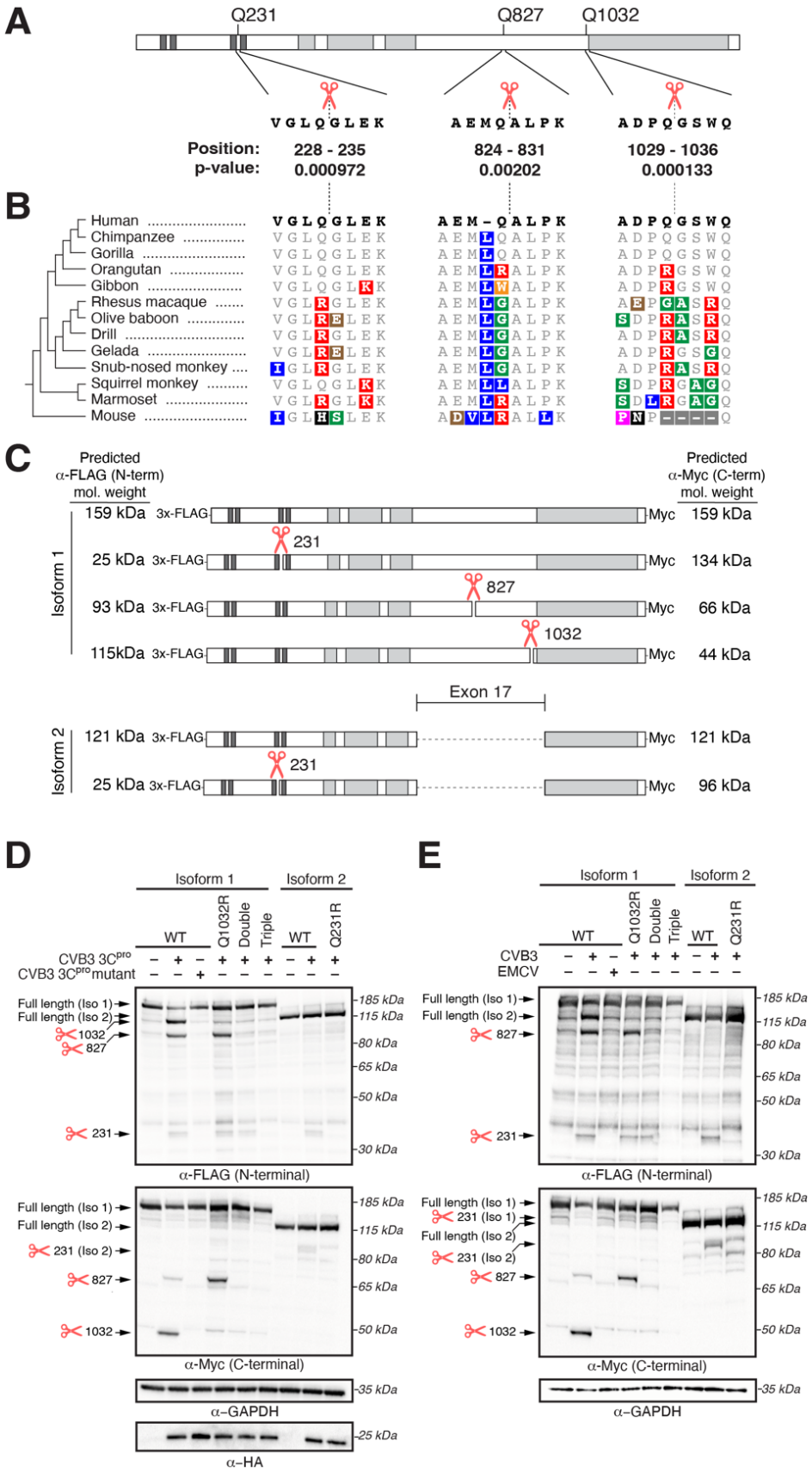

Figure 4. NINL is cleaved at species-specific sites by virally encoded proteases. (**A**) Schematic of human NINL, with positions of predicted 3C^{pro} cleavage sites annotated. Shown are the four amino acids

on each side of the predicted cleavage site in human NINL, along with the residue positions and cleavage score predicted using a motif search with the consensus enterovirus cleavage site (see Methods). (**B**) NINL sequences from 12 primate species and mice for each predicted $3C^{pro}$ cleavage site. Amino acid changes relative to human NINL are highlighted in colors to denote differences in polarity and charge. (**C**) Schematic of 3xFLAG-NINL-Myc isoform 1 and isoform 2 constructs, with predicted molecular weights for both amino-terminal (FLAG) and carboxy-terminal (Myc) products upon cleavage by $3C^{pro}$. (**D**) Immunoblots of extracts from HEK293T cells co-transfected with the indicated NINL constructs and either CVB3 $3C^{pro}$ or the catalytically inactive (C147A) CVB3 $3C^{pro}$ (mutant). Immunoblots were probed with anti-FLAG (NINL amino-terminus), anti-Myc (NINL carboxy-terminus), anti-HA ($3C^{pro}$), and anti-GAPDH (loading control). Arrows to the left of each immunoblot indicate full-length products as well as products corresponding to cleavage at the indicated amino acid residue. Protein molecular weight markers are shown in kilodaltons (kDa) to the right of each immunoblot. Representative images from three biological replicates are shown. (**E**) Immunoblots of extracts from HEK293T cells transfected with the indicated amino-terminal FLAG and carboxyl-terminal Myc tagged NINL constructs and infected with either CVB3 or EMCV (500,000 PFU/mL, MOI ≈ 1.0 for 8 h). Immunoblots were probed with anti-FLAG (NINL amino-terminus), anti-Myc (NINL carboxy-terminus), and anti-GAPDH (loading control). Arrows to the left of each immunoblot indicate full length products as well as products corresponding to CVB3 $3C^{pro}$ cleavage at the indicated amino acid residue. Protein molecular weight markers are shown in kilodaltons (kDa) to the right of each immunoblot. Representative images from three biological replicates are shown.

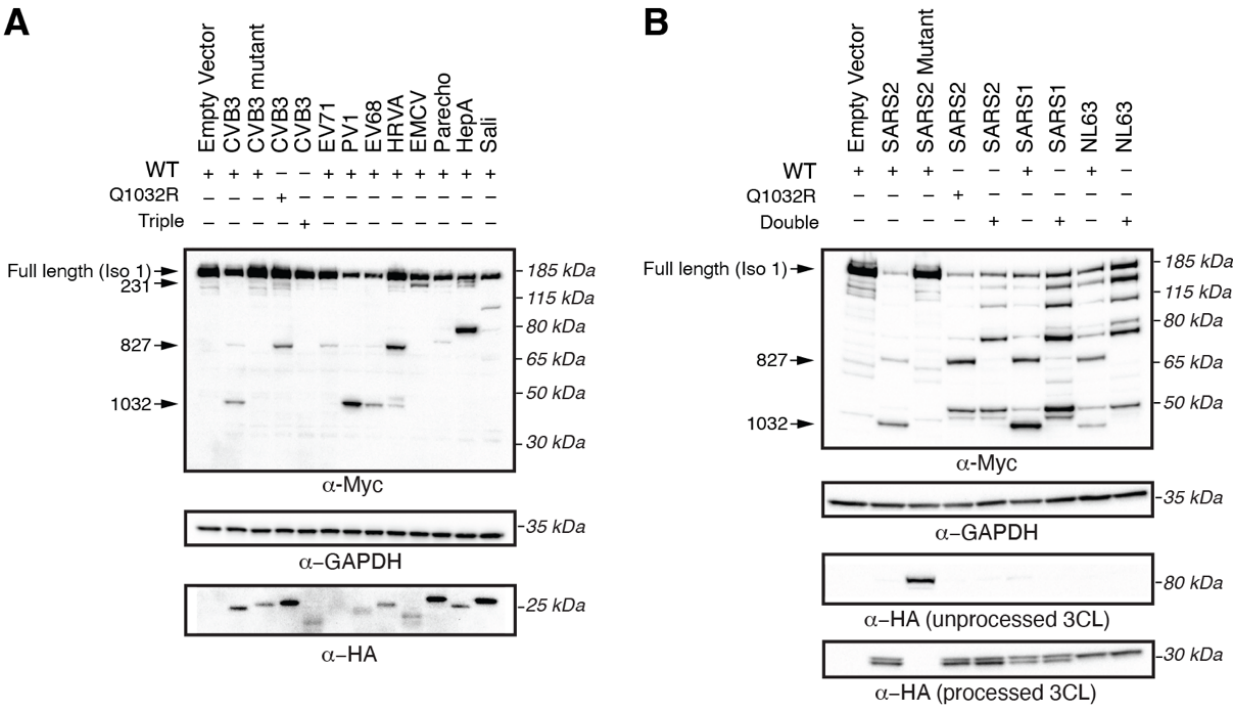

Figure 4–figure supplement 1. **3C and 3CL proteases from diverse viruses cleave NINL at redundant and unique sites.** (**A**) Immunoblots of extracts from HEK293T cells co-transfected with the indicated NINL constructs and $3C^{pro}$ from the indicated picornavirus. CVB3: coxsackievirus B3, CVB3 mutant: catalytically inactive (C147A) CVB3 $3C^{pro}$, EV71: enterovirus A71, PV1: poliovirus 1, EV68: enterovirus D68, HRVA: human rhinovirus A, EMCV: encephalomyocarditis virus, Parecho: parechovirus A, HepA: hepatitis A virus, Sali: salivirus A. Immunoblots were probed with anti-Myc (NINL carboxy-terminus), anti-HA ($3C^{pro}$), and anti-GAPDH (loading control). Arrows to the left of each immunoblot indicate full-length products as well as products corresponding to CVB3 $3C^{pro}$ cleavage at the indicated amino acid residue. Protein molecular weight markers are shown in kilodaltons (kDa) to the right of each immunoblot. Representative images from three biological replicates are shown. (**B**) Immunoblots of extracts from HEK293T cells co-transfected with the indicated NINL constructs and the indicated coronaviral $3CL^{pro}$. SARS2: SARS-CoV-2, SARS2 mutant: catalytically inactive (C145A) SARS-CoV-2 $3CL^{pro}$ SARS1: SARS-CoV, NL63: HCoV-NL63. $3CL^{pros}$ were expressed as self-cleaving constructs that remove a carboxy-terminal mCherry-HA tag. Immunoblots were probed with anti-Myc (NINL carboxy-terminal), anti-HA (cleaved mCherry-HA from catalytically active protease constructs, or eGFP-$3CL^{pro}$-mCherry-HA from catalytically inactive protease constructs), and anti-GAPDH (loading control). Arrows to the left of each immunoblot indicate full-length products as well as products corresponding to SARS-CoV-2 $3CL^{pro}$ cleavage at the indicated amino acid residue. Protein molecular weight markers are shown in kilodaltons (kDa) to the right of each immunoblot. Representative images from three biological replicates are shown.

transfected with CVB3 $3C^{pro}$, although we did observe weak protease-mediated cleavage at site 231 in isoform 2 (Figure 4D).

We next sought to understand the degree to which cleavage of NINL is conserved across viral proteases. We, therefore, tested a panel of $3C^{pros}$ from diverse viruses in the *Picornaviridae* family (Tsu et al., 2021a). Interestingly, while we found that all proteases tested were able to cleave NINL to some degree, the strength and position of cleavage was variable, even among proteases from closely related viruses such CVB3, enterovirus 71 (EV71), poliovirus (PV1), enterovirus D68 (EV68), and human rhinovirus A (HRVA), all of which are members of the enterovirus genus (Figure 4–figure supplement 1A). We also tested a panel of 3C-like proteases ($3CL^{pros}$) from members of the *Coronaviridae* family, including proteases from the betacoronaviruses, SARS-CoV-2 and SARS-CoV, and an alphacoronavirus, NL63-CoV. We again observed numerous cleavage products, some of which map to residues 827 and 1032 (Figure 4–figure supplement 1B), consistent with $3C^{pros}$ and $3CL^{pros}$ having similar active sites and cleavage preferences (Ng et al., 2021). Together, these data indicate that NINL is cleaved at species-specific sites by various proteases from human viruses. Such host- and virus-specificity of cleavage is a hallmark of host-virus arms races, further supporting the model that NINL's role in the interferon response positions it in evolutionary conflict with viruses.

We next aimed to confirm that infection-mediated cleavage efficiency and specificity recapitulated results we observed from transiently transfected viral proteases. We therefore infected cells expressing WT NINL and the NINL triple mutant with CVB3, a virus that encodes a $3C^{pro}$ that strongly cleaves NINL at multiple sites, and EMCV, a virus that encodes a $3C^{pro}$ that only weakly cleaves NINL at a single site in the N-terminus (Figure 4–figure supplement 1A). Consistent with the results we obtained with transfected $3C^{pros}$, we observed cleavage of NINL at species-specific sites 231, 827, and 1032 when we infected with CVB3, and little to no cleavage upon EMCV

infection (Figure 4E). These data further support that NINL is a target of viral antagonism upon infection in a manner that is both host- and virus-specific.

Viral proteases disrupt NINL trafficking function

As NINL is a dynein activating adaptor, we next sought to investigate whether proteolytic cleavage of NINL could interfere with cargo trafficking. NINL is well known as a centrosome-associated protein and may also be involved in trafficking endo/lysosomal membranes (Bachmann-Gagescu et al., 2015; Xiao et al., 2021). In addition, a number of NINL-interacting proteins have been described (Bachmann-Gagescu et al., 2015; Casenghi et al., 2003; Dona et al., 2015; Kersten et al., 2012; Redwine et al., 2017; van Wijk et al., 2009). However, in the context of the interferon response, we have not yet identified a NINL cargo. Thus, we chose to reconstitute NINL's role in dynein-mediated microtubule transport using a heterologous approach (Kapitein et al., 2010; Passmore et al., 2021). This well-established method uses an inducible heterodimerization system (Figure 5A) to induce the movement of normally immotile peroxisomes by recruiting dynein via an activating adaptor to the peroxisome (Htet et al., 2020; Huynh and Vale, 2017; Wang et al., 2019). Briefly, a rapamycin-binding FKBP domain was targeted to peroxisome membranes via the peroxisome targeting sequence (PTS1) of human PEX3. Another rapamycin-binding FRB domain was fused to the NINL and the NINL triple mutant constructs. We truncated the NINL constructs at residue 1062 because some activating adaptors are autoinhibited via interactions between their amino- and carboxy-termini (Liu et al., 2013; Terawaki et al., 2015; Urnavicius et al., 2015). Co-transfection of cells with CVB3 $3C^{pro}$, PEX3-mEmerald-FKBP, and WT NINL or the uncleavable NINL triple mutant confirmed that WT NINL is cleaved by CVB3 $3C^{pro}$, while the NINL triple mutant is not (Figure 5B and Figure 5–figure supplement 1A). When we introduced these constructs into human U-2 OS cells peroxisomes were distributed throughout the cytoplasm (Figure 5C and Figure 5–figure supplement 1B, C), but redistributed to the centrosome upon the addition of the rapamycin analog, rapalog (which induces dimerization of

FRB and FKBP (Ho et al., 1996) (Figure 5C-E). In contrast, when NINL was co-expressed with CVB3 $3C^{pro}$, peroxisomes no longer localized to the centrosome (Figure 5C-E). However, the uncleavable NINL triple mutant was still able to redistribute peroxisomes in the presence of CVB3 $3C^{pro}$ just as effectively as U-2 OS cells not expressing CVB3 $3C^{pro}$ (Figure 5C-E). Finally, to determine if viral infection could also disrupt NINL-mediated trafficking, we infected cells with CVB3 following transfection of PEX3-mEmerald-FKBP, and WT NINL or the uncleavable NINL triple mutant. Similar to transfection with viral protease, live CVB3 infection led to a significant reduction in peroxisomes that localized to the centrosome in cells expressing NINL, but not in cells expressing the uncleavable NINL triple mutant (Figure 6A, B and Figure 6–figure supplement 1A, B). Together, these data demonstrate that site-specific cleavage of NINL by CVB3 $3C^{pro}$ could disrupt NINL's role in cargo transport.

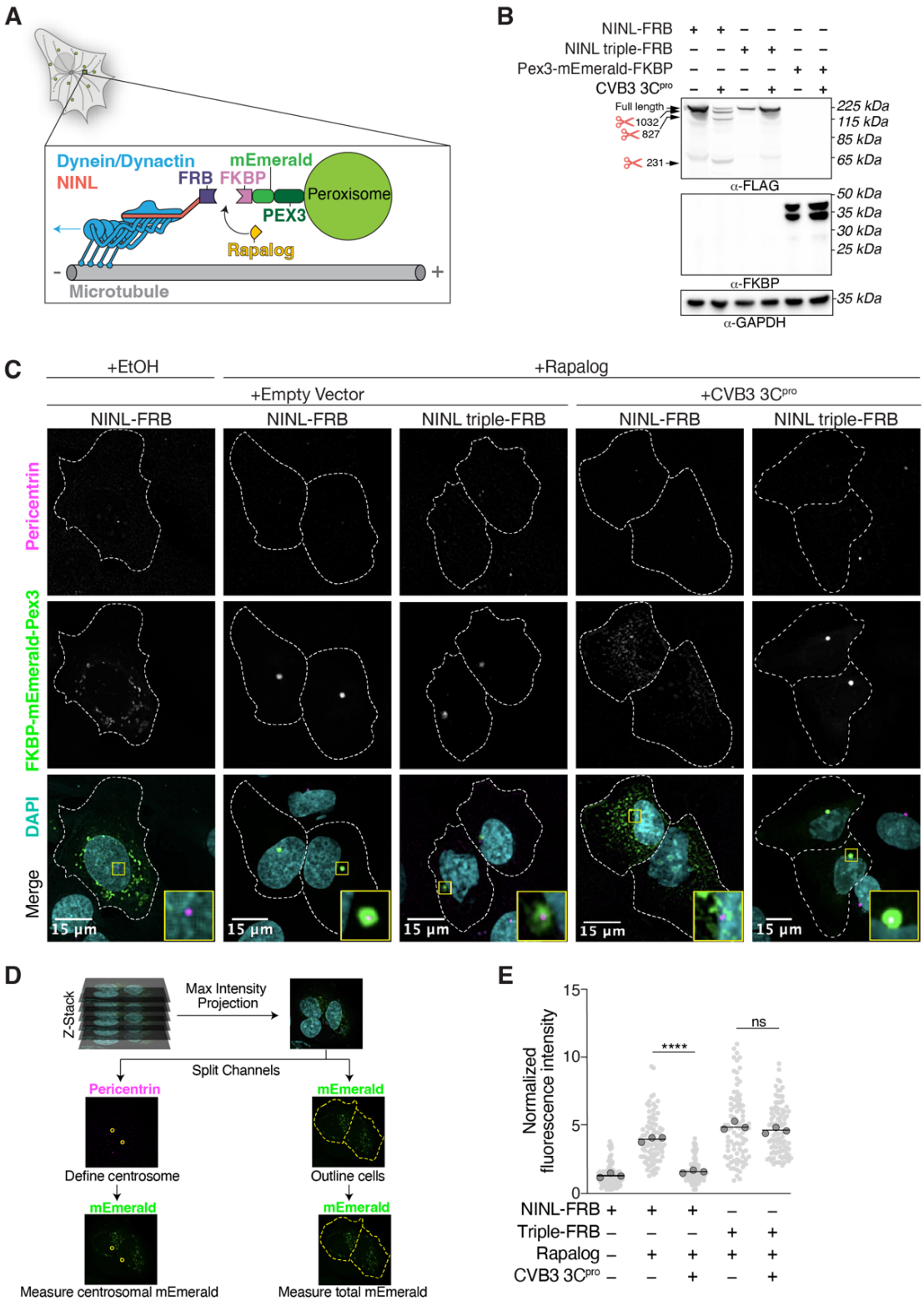

Figure 5. CVB3 3C^{pro} cleavage of NINL prevents rapalog-induced dynein-dependent transport of intracellular cargoes. (**A**) Schematic of the peroxisomal trafficking assay. The peroxisomal targeting signal (PTS1) of human PEX3 (amino acids 1–42) was fused to mEmerald and FKBP and a truncated NINL (amino acids 1-1062) was fused to FRB. Dynein-dependent accumulation of peroxisomes at the centrosome, where most minus-ends are located, is initiated by the rapalog-mediated heterodimerization of FKBP and FRB. Blue arrow indicates dynein motility. (**B**) Indicated FRB and FKBP

constructs transiently expressed with (+) or without (-) the transient co-expression of HA-tagged CVB3 $3C^{pro}$ in HEK293T cells. Immunoblots were probed with anti-FLAG, anti-FKBP, anti-GAPDH and anti-HA antibodies. Protein molecular weight markers are shown in kilodaltons (kDa) to the left of each immunoblot. Representative images from three biological replicates are shown. (**C**) Confocal micrographs are displayed as maximum intensity projections of U-2 OS cells, transfected with Pex3-mEmerald-FKBP and the indicated cleavable or uncleavable NINL-FRB fusion constructs with or without the co-expression of CVB3 $3C^{pro}$. Where indicated, cells were treated for one hour with ethanol (EtOH) as a control or 1 μM rapalog in EtOH prior to fixation. Centrosomes were immunostained with anti-pericentrin and nuclei were visualized with DAPI. 15 μm scale bars indicated in lower left corner of merged micrographs. Yellow rectangles denote region of cropped inset. Dashed white lines denote cellular boundaries. Representative micrographs from three biological replicates are shown. (**D**) Schematic of the analysis pipeline. (**E**) Quantification of peroxisomal trafficking assays from three biological replicates. The fluorescence intensity of Pex3-mEmerald-FKBP at the centrosome was normalized to the whole-cell fluorescence, and to the areas of the regions of interest used to quantify centrosome versus whole-cell fluorescence. Each datapoint corresponds to an individual cell. The dark grey, large, outlined circles correspond to the mean for each biological replicate. For each condition n = ~80. The mean across all replicates is denoted by the bold line. Data were analyzed using Kruskal–Wallis with Dunn's post hoc test for multiple comparisons. ****$p<0.0001$, ns = not significant.

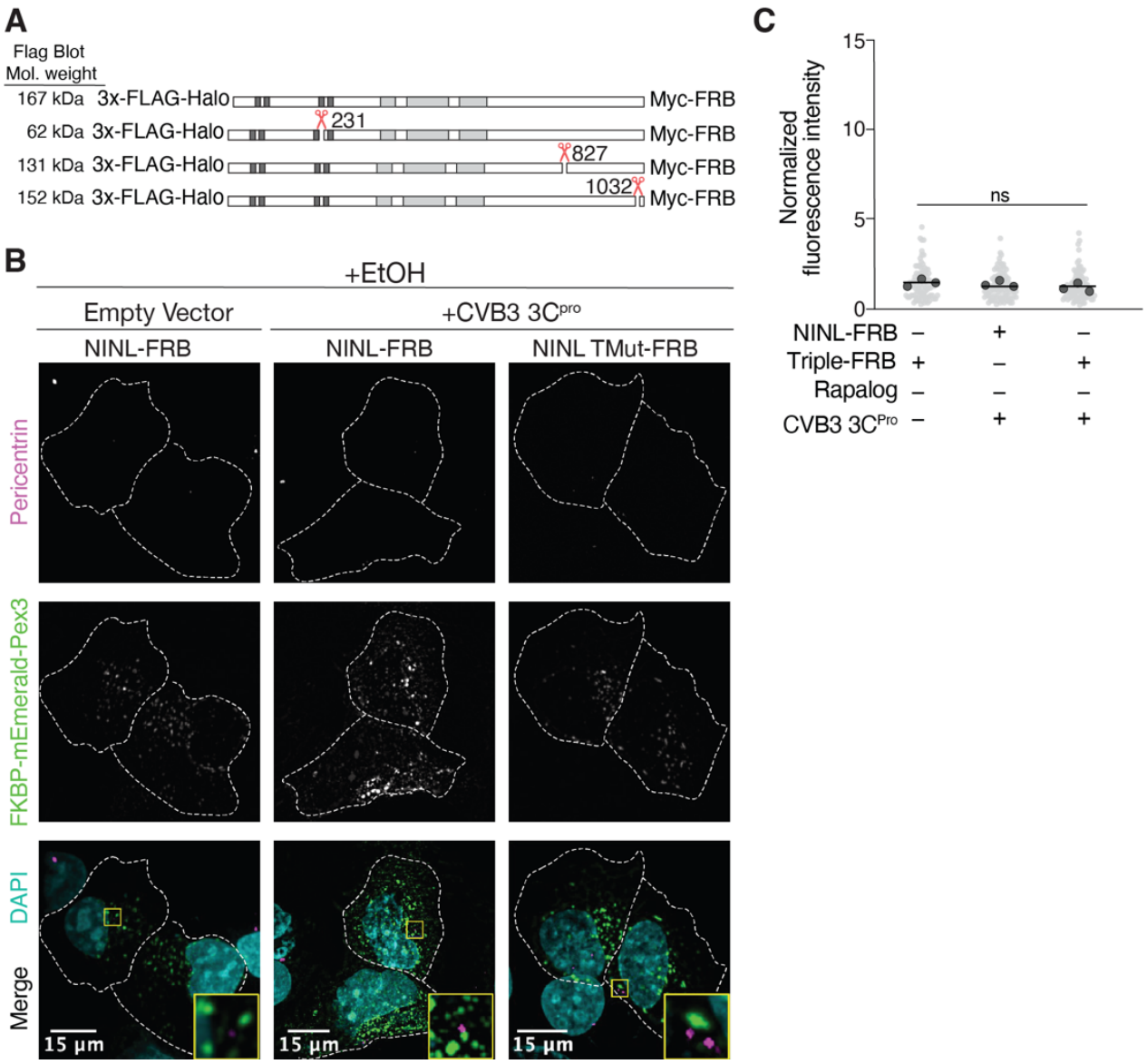

Figure 5–figure supplement 1. Peroxisome distribution remains consistent regardless of presence of CVB3 3C^{pro} prior to rapalog induced dynein-dependent transport. (**A**) Schematic of NINL-FRB fusion constructs. Predicted molecular weights for each 3xFLAG tagged amino-terminal cleavage product produced by 3C^{pro}. (**B**) Peroxisome distribution controls. Confocal micrographs displayed as maximum intensity projections of U-2 OS cells, transfected with Pex3-mEmerald-FKBP and the indicated cleavable or uncleavable NINL-FRB fusion constructs with or without the co-expression of CVB3 3C^{pro} treated for one hour with ethanol (EtOH) prior to fixation. Centrosomes were immunostained with anti-pericentrin and nuclei were visualized with DAPI. 15 µm scale bars are indicated in the lower left corner of the merged micrographs. Yellow rectangles denote region of cropped inset. Dashed white lines denote cellular boundaries. Representative micrographs from three biological replicates are shown. (**C**) Quantification of peroxisomal trafficking assay from three biological replicates. The fluorescence intensity of Pex3-mEmerald-FKBP at the centrosome was normalized to the whole-cell fluorescence, and to the areas of the regions of interest used to quantify centrosome versus whole-cell fluorescence. Each datapoint corresponds to an individual cell and biological replicates can be distinguished by shade. For each condition n = ~80. The mean across all replicates is denoted by the bold line. Bold circles correspond to the mean for each biological replicate. Data were analyzed using Kruskal–Wallis with Dunn's post hoc test for multiple comparisons. ns = not significant.

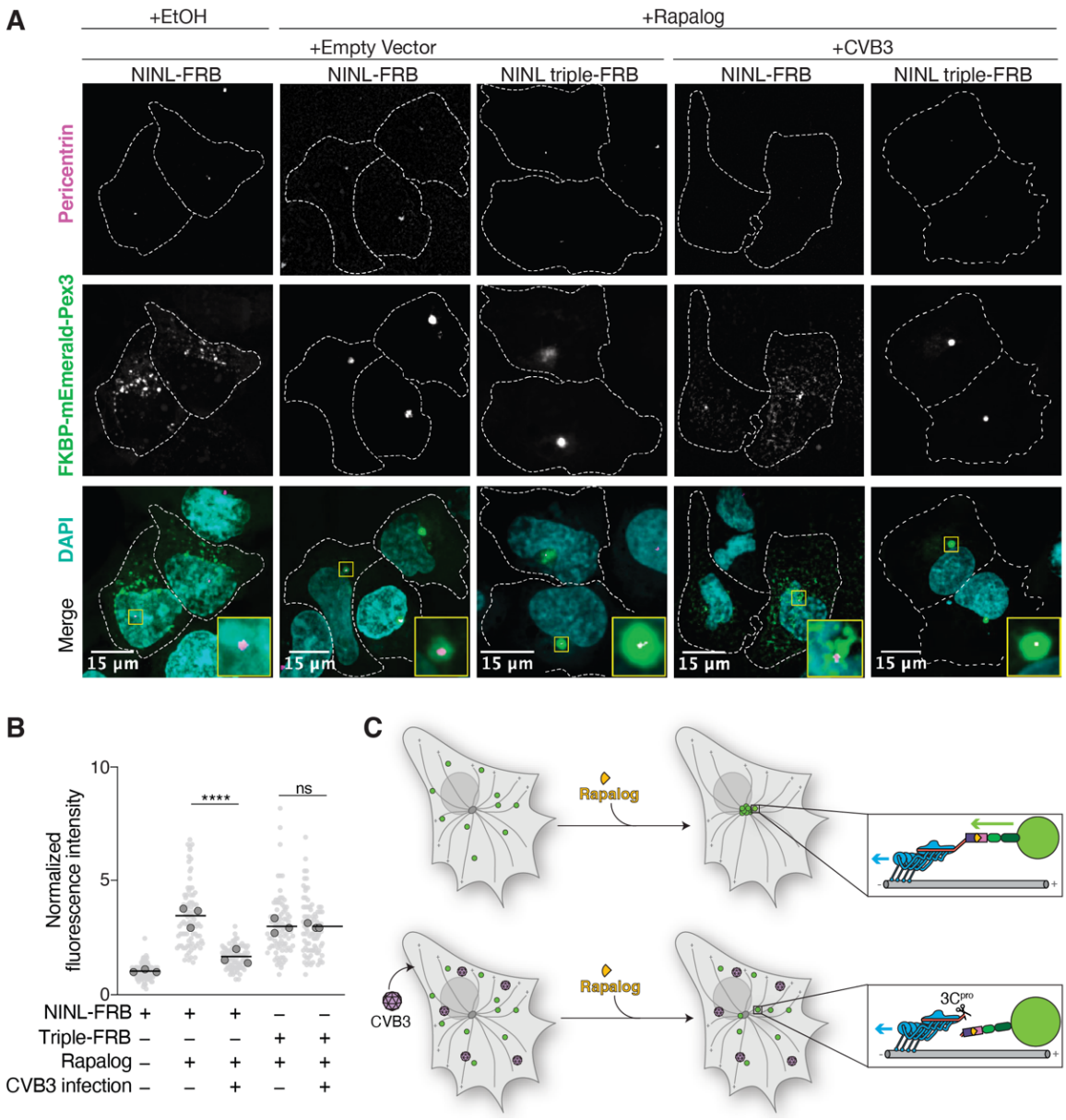

Figure 6. Cleavage of NINL during viral infection prevents dynein-dependent transport of an intracellular cargo. (**A**) Confocal micrographs displayed as maximum intensity projections of uninfected or CVB3 infected U-2 OS cells. Cells were transfected with Pex3-mEmerald-FKBP and the indicated cleavable or uncleavable NINL-FRB fusion constructs, and infected (or mock infected) with CVB3 (500,000 PFU/ml, MOI = ~2) for five hours. Cells were then treated for one hour with ethanol (EtOH) or 1 µM rapalog prior to fixation. Centrosomes were immunostained with anti-pericentrin and nuclei were visualized with DAPI. 15 µm scale bars are indicated in the lower left corner of the merged micrographs. Yellow rectangles denote region of cropped inset. Dashed white lines denote cellular boundaries. Representative micrographs from three biological replicates are shown. (**B**) Quantification of peroxisomal trafficking assays from three biological replicates. The fluorescence intensity of Pex3-mEmerald-FKBP at the centrosome was normalized to the whole-cell fluorescence, and to the areas of the regions of interest used to quantify centrosome versus whole-cell fluorescence. Each datapoint corresponds to an individual cell and biological replicates can be distinguished by shade. For each condition n = ~80. The mean across all replicates is denoted by the bold line. Bold circles correspond to the mean for each biological replicate. Data were analyzed using Kruskal–Wallis with Dunn's post hoc test for multiple comparisons. ****p<0.0001, ns = not significant. (**C**) Schematic of the rapalog-induced pericentrosomal accumulation of peroxisomes and loss of accumulation upon viral infection.

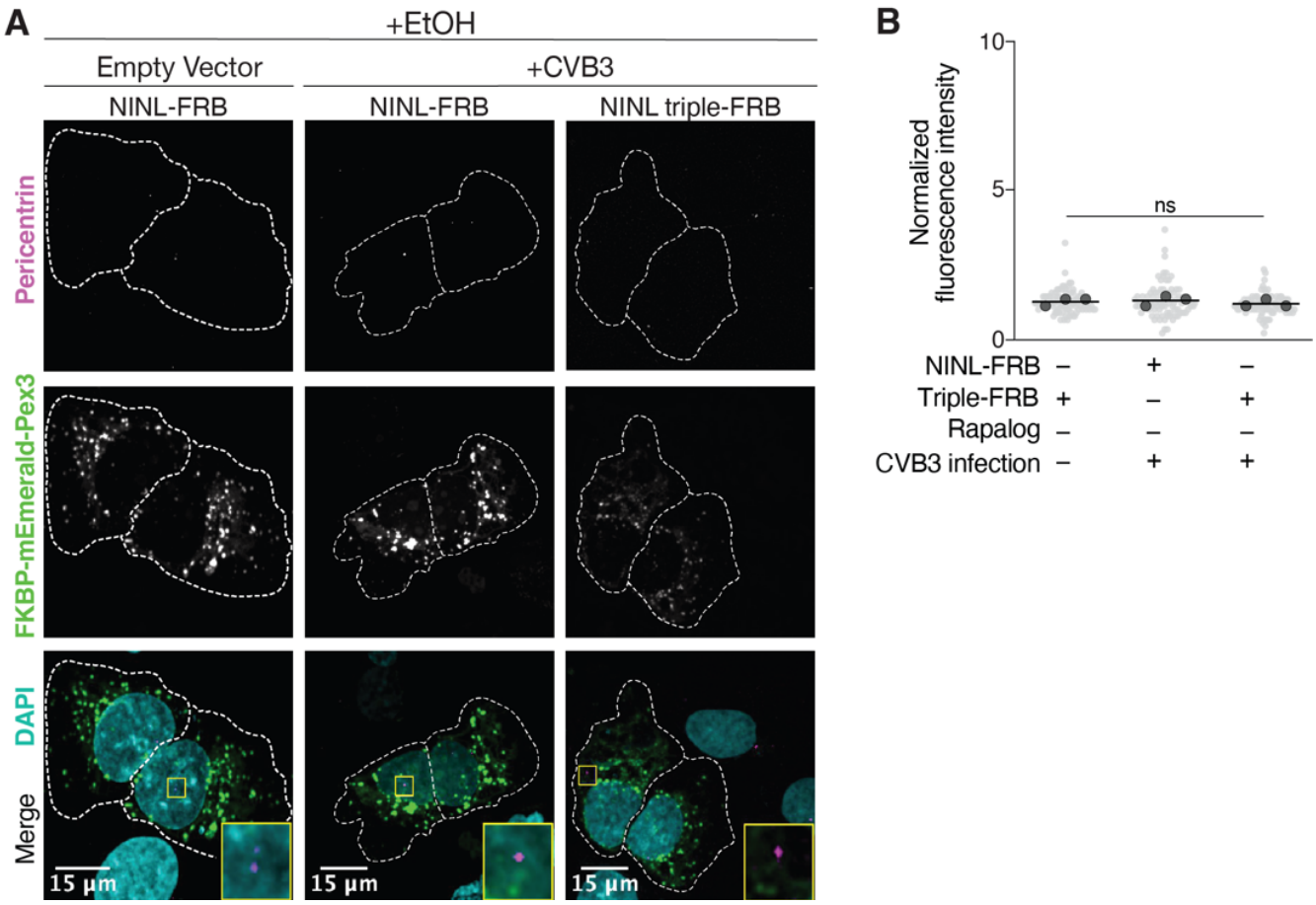

Figure 6–figure supplement 1. Peroxisome distribution remains consistent regardless of CVB3 infection prior to rapalog induced dynein-mediated transport. (**A**) Peroxisome distribution controls. Confocal micrographs displayed as maximum intensity projections of uninfected or CVB3 infected U-2 OS cells expressing Pex3-mEmerald-FKBP and the indicated cleavable or uncleavable NINL-FRB fusion constructs treated for one hour with ethanol (EtOH) prior to fixation. Centrosomes were immunostained with anti-pericentrin and nuclei were stained with DAPI. 15 µm scale bars are indicated in the lower left corner of the merged micrographs. Yellow rectangles denote region of cropped inset. Dashed white lines denote cellular boundaries. Representative micrographs from three biological replicates are shown. (**B**) Quantification of peroxisomal trafficking assays from three biological replicates. Fluorescence intensity of Pex3-mEmerald-FKBP at the centrosome was normalized to the whole-cell fluorescence, and to the areas of the regions of interest used to quantify centrosome versus whole-cell fluorescence. Each datapoint corresponds to an individual cell and biological replicates can be distinguished by shade. For each condition n = ~80. The mean across all replicates is denoted by a bold line. Bold circles correspond to the mean for each biological replicate. Data were analyzed using Kruskal–Wallis with Dunn's post hoc test for multiple comparisons. ns = not significant.

Discussion

Pathogenic viruses and their hosts are engaged in genetic conflicts at every step of the viral life cycle. Each of these points of conflict, which center on direct interactions between viral and host proteins, have the potential to determine the degree to which a virus replicates and causes pathogenesis in a host cell, and the degree to which the immune system can inhibit viral replication. As such, evolutionary adaptation in both host and viral genomes shape these molecular interactions, leaving behind signatures of rapid evolution that can serve as beacons for points of host-virus interaction (Daugherty and Malik, 2012; Duggal and Emerman, 2012; Tenthorey et al., 2022). Here we use this evolutionary principle to reveal an antiviral role for the dynein activating adaptor NINL. Unique among 36 analyzed dynein, dynactin, and activating adaptor genes, we found that NINL displays a signature of recurrent positive selection in primates. Based on this unusual evolutionary signature in an otherwise highly conserved cellular machine, we hypothesized that NINL may be engaged in an undescribed host-pathogen conflict. Using multiple cell types and knockout clones, we reveal that loss of NINL results in reduced activation of the antiviral innate immune response following IFNα treatment. Consequently, in NINL KO cells several RNA and DNA viruses show significantly increased replication after IFNα pretreatment relative to WT cells. These results indicate NINL plays an important role in the antiviral immune response.

Further work will be required to determine the mechanistic basis for NINL's antiviral function. The role of activating adaptors in inducing processive dynein motility was only described in 2014 (McKenney et al., 2014; Schlager et al., 2014). Since that time, the number of established activating adaptors has rapidly expanded, as has our understanding of the molecular interactions between activating adaptors and dynein/dynactin (Agrawal et al., 2022; Cason et al., 2021; Chaaban and Carter, 2022; Fenton et al., 2021; Lau et al., 2021; Lee et al., 2020; Olenick and

Holzbaur, 2019; Reck-Peterson et al., 2018). However, for many activating adaptors, including NINL, much less is known about cargo specificity. Our observation that NINL KO cells have a defect in ISG production following IFNα treatment, despite normal phosphorylation of the STAT1 and STAT2 transcription factors, suggests a role for NINL in the IFN signaling pathway. These results are consistent with recent gene enrichment analyses implicating NINL in several immune pathways, including JAK-STAT signaling (Chen et al., 2022). However, whether a signaling complex is a direct cargo of NINL, or whether NINL's interaction with dynein and dynactin is required for this function, remain to be determined. Notably, we observe several transcriptional changes in NINL KO cells relative to WT cells, suggesting that NINL plays regulatory roles in the cell beyond our observation of its role in the IFN effect. Like other activating adaptors, understanding the full range of cargos and biological functions of NINL will require additional studies.

Despite the uncertainty of NINL's mechanistic role in the antiviral immune response, we find that several viruses can antagonize NINL function through proteolytic cleavage. Using the model enterovirus, CVB3, we show that the virally-encoded 3C protease ($3C^{pro}$) cleaves human NINL at three independent sites, all of which toggle between cleavable and uncleavable even among closely related primates. These changes within the cleavage sites of NINL in primates suggest that virally-encoded proteases are one potential evolutionary pressure that is driving the rapid evolution of NINL, similar to other molecular arms races between viral proteases and host proteins (Tsu et al., 2021b). Related $3C^{pros}$ from other picornaviruses, as well as $3CL^{pros}$ from coronaviruses, also cleave NINL. Intriguingly, even closely related proteases, for instance $3C^{pros}$ within the enterovirus clade, have different site preferences within NINL, suggesting that viral protease evolution may be shaping its interactions with NINL. Indeed, among the diversity of picornavirus and coronavirus proteases we tested, we find that that NINL cleavage is almost universally maintained despite a wide array of site preferences and cleavage efficiencies. These

data indicate that numerous viral proteases convergently cleave NINL, reminiscent of other convergently antagonized targets in the innate antiviral response such as MAVS, TRIF, and NEMO (Tsu et al., 2021b). Compellingly, cleavage of NINL by $3C^{pro}$ during viral infection disrupts the NINL-mediated transport of a heterologous cargo. Along with our data indicating that one function of NINL is to potentiate the innate immune response, these data suggest that cleavage of NINL could be a host-specific mechanism employed by viruses to disrupt the antiviral immune response and promote their own replicative success.

Altogether, our study demonstrates the effectiveness of leveraging genetic signatures of pathogen-driven evolution to identify new components of host innate immunity. Our insights into the conflict between viruses and NINL provides a glimpse into the impact that viruses may have on the evolution of the intracellular transport machinery and identify a new role for a dynein activating adaptor in the antiviral immune response. These results indicate that components of the otherwise conserved cytoplasmic dynein transport machinery can be engaged in host- and virus-specific interactions and suggest intracellular transport could be an important battleground for host-virus arms races.

Materials and Methods

Evolutionary analysis

For evolutionary analyses of dynein, dynactin, and activating adaptor genes, Uniprot reference protein sequences were used as a search query against NCBI's non-redundant (NR) database using tBLASTn (Altschul et al., 1990). For each primate species, the nucleotide sequence with the highest bit score was downloaded and aligned to the human ORF nucleotide sequence using MAFFT (Katoh, 2002) implemented in Geneious software (Dotmatics; geneious.com). Poorly aligning sequences or regions were removed from subsequent analyses. Maximum likelihood

(ML) tests were performed with codeml in the PAML software suite (Yang, 2007). Aligned sequences were subjected to ML tests using NS sites models disallowing (M7) or allowing (M8) positive selection. The p-value reported is the result of a chi-squared test on twice the difference of the log likelihood (lnL) values between the two models using two degrees of freedom. Analyses were performed using two models of frequency (F61 and F3x4) and both sets of values are reported. For each codon model, we confirmed convergence of lnL values by performing each analysis using two starting omega (dN/dS) values (0.4 and 1.5). For evolutionary analyses of the isolated NINL amino-terminal (dynein/dynactin binding) and carboxy-terminal (cargo binding) regions, the full-length alignment was truncated to only include codons 1-702 or 703-1382 respectively and PAML analyses were performed as described above.

We used three independent methods to estimate codons within NINL that have been subject to positive selection. PAML was used to identify positively selected codons with a posterior probability greater than 0.90 using a Bayes Empirical Bayes (BEB) analysis and the F61 codon frequency model. The same NINL alignment was also used as input for FEL (Kosakovsky Pond and Frost, 2005) and MEME (Murrell et al., 2012) using the DataMonkey (Weaver et al., 2018) server. In both cases, default parameters were used and codons with a signature of positive selection with a p-value of <0.1 are reported. In all cases, codon numbers correspond to the amino acid position and residue in human NINL (NCBI accession NM_025176.6).

Molecular cloning

For the plasmid-based CRISPR/Cas9-mediated knockout of NIN and NINL we designed gRNA target sequences with the web tool CHOPCHOP (Labun et al., 2016), available at chopchop.cbu.uib.no, and synthesized oligonucleotides from Eton Biosciences (San Diego, CA, USA). Each oligonucleotide pair was phosphorylated and annealed using the T4 Polynucleotide Kinase (New England Biolabs, Ipswich, MA, USA). Duplexed oligonucleotides were ligated into

BbsI (New England Biolabs) digested pSpCas9(BB)-2A- Puro (pX459) V2.0, a gift from Feng Zhang (Addgene plasmid #62988), using the Quick Ligase kit (New England Biolabs). For cleavage assays, the coding sequence of human NINL isoform 1 (NCBI accession NM_025176.6) was subcloned from the previously described pcDNA5/FRT/TO-BioID-NINL-3xFLAG (Redwine et al., 2017) and inserted into pcDNA5/FRT/TO with as part of the following cassette: mCherry-P2A-3xFLAG-NINL-Myc. NINL mutants (Q1032R, Q827/1032R, Q231/827/1032R), human NINL isoform 2 (NCBI accession NM_001318226.2) and the NINL isoform 2 mutant (Q231R) were mutagenized using the Q5 Site-Directed Mutagenesis Kit (New England BioLabs). The plasmids encoding 3C proteases (coxsackievirus B3 (CVB3) $3C^{pro}$, catalytically inactive (C147A) CVB3 $3C^{pro}$, enterovirus A71 (EV71) $3C^{pro}$, poliovirus 1 (PV1) $3C^{pro}$, enterovirus D68 (EV68) $3C^{pro}$, human rhinovirus A (HRVA) $3C^{pro}$, encephalomyocarditis virus (EMCV) $3C^{pro}$, parechovirus A (Parecho) $3C^{pro}$, hepatitis A virus (HepA) $3C^{pro}$, and salivirus A (Sali) $3C^{pro}$) have been described previously (Tsu et al., 2021a). To ensure that $3CL^{pros}$ have precise amino- and carboxy-termini as a result of self-cleavage, sequences for 3CL proteases (SARS2 $3CL^{pro}$, SARS1 $3CL^{pro}$, and NL63 $3CL^{pro}$), including nine residues from the upstream coding region (nsp4) and downstream coding region (nsp6) were ordered as gBlocks (Integrated DNA Technologies, Coralville, IA) (Supplementary File 5) and cloned into the pQCXIP backbone flanked by an N-terminal eGFP and a C-terminal mCherry-HA sequence. Catalytically inactive (C145A) SARS2 $3CL^{pro}$ was made using overlapping stitch PCR. For the peroxisome trafficking assay, the peroxisomal membrane-targeting sequence (amino acids 1–42) of human PEX3 (NCBI accession NM_003630) with a carboxy-terminal mEmerald fluorescent protein and FKBP was subcloned from the previously described pcDNA5-PEX3-Emerald-FKBP (Htet et al., 2020) and into the pcDNA3.1(+) backbone. 3xFLAG-Halo-NINL(1-1062)-Myc-FRB was synthesized as a gBlock (Integrated DNA Technologies) and cloned into the pcDNA3.1(+) backbone. To generate an uncleavable mutant of this construct we used sequential Q5 mutagenesis to achieve Q231/827/1032R. Following cloning, all plasmids were verified with whole plasmid sequencing. Plasmids and primers used in

this study can be found in Supplementary File 5. All newly created plasmids will be made available upon request.

Transfections

All transfections in this study were performed with TransIT-X2® Transfection Reagent (Mirus Bio, Madison, WI, USA) according to the manufacturer's instructions. Briefly, 18-24 hours prior to transfection the desired cells were plated at an appropriate density such that they would be ≥80% confluent at time of transfection. TransIT-X2:DNA complexes were formed following the manufacturer's protocol. The TransIT-X2:DNA complexes were then evenly distributed to cells via drop-wise addition and were incubated in a humidified 5% CO2 atmosphere at 37°C for until they were harvested, assayed, or placed into selection as described below.

Cell lines

All cell lines used in this study were sourced from the American Type Culture Collection (ATCC; Manassas, VA) unless otherwise indicated and maintained in a humidified 5% CO_2 atmosphere at 37°C. All cell lines are routinely tested for mycoplasma by PCR kit (ATCC). HEK293T (human embryonic kidney epithelial cells, ATCC CRL-3216), A549 (human alveolar adenocarcinoma cells, ATCC CCL-185), U-2 OS (human epithelial osteosarcoma cells, ATCC HTB-96), BSC40 (grivet kidney epithelial cells, ATCC CRL-2761), Vero (African green monkey kidney epithelial cells, ATCC CCL-81), and BHK-21 (Syrian golden hamster kidney fibroblast cells, ATCC CCL-10) were maintained in complete growth media which is composed of Dulbecco's Modified Eagle's Medium with 4.5g/L glucose, L-glutamine, and sodium pyruvate (DMEM; Corning, Manassas, VA, USA) supplemented with 10% (v/v) fetal bovine serum (FBS; Gibco, Grand Island, NY, USA) and 1% (v/v) Penicillin/Streptomycin (PenStrep; Corning). Flp-In™ T-REx™ HCT116 (human colorectal carcinoma cells) were a gift from E. Bennett at the University of California San Diego (La Jolla, CA, USA) but originated in the laboratory of B. Wouters at the University of Toronto

(Toronto, ON, Canada) and were maintained in complete growth media supplemented with 100 μg/ml Zeocin. Cells are routinely tested for mycoplasma contamination using mycoplasma by PCR kit (ATCC, Manassas, VA) and kept at low passage to maintain less than one year since acquisition or generation.

CRISPR/Cas9-mediated gene editing

To generate NIN and NINL knock outs in A549, HCT116 and U-2 OS cell lines, the cells were transfected with 250 ng of the pX459 vector containing the appropriate gRNAs. Transfected cells were enriched 48 hours post-transfection by culturing them with complete growth media supplemented with 1 μg/ml puromycin for 48 hours and then were allowed to recover for 24 hours in complete growth media without puromycin. Following enrichment of transfected cells, monoclonal cell lines were obtained by expanding single-cell clones isolated by limiting dilution. The resulting clones were screened via immunoblotting with gene-specific antibodies anti-NINL rabbit polyclonal antibody (Thermo Fisher Scientific, Waltham, MA,USA) and anti-NIN mouse monoclonal antibody (LSBio, Seattle, WA, USA). Clones determined to be knockouts via immunoblotting were screened further to confirm the presence of CRISPR-induced indels in each allele of the targeted gene. Genomic DNA was isolated using the *DNeasy Blood & Tissue Kit* (Qiagen, Hilden, Germany) and the target exons were amplified with Econo*Taq* polymerase (Lucigen, Middleton, WI, USA). The resulting amplicons were subcloned using the TOPO TA Cloning Kit for Sequencing (Thermo Fisher Scientific) and transformed into DH5α competent cells. Single colonies were picked, and the plasmids were isolated by miniprep (Qiagen) and sequenced individually using T3 and T7-Pro primers. All newly created cell lines will be made available upon request.

Immunoblotting

Harvested cell pellets were washed with 1X PBS, and unless otherwise noted, lysed with RIPA lysis buffer: 50 mM 2-Amino-2-(hydroxymethyl)propane-1,3-diol (Tris), pH 7.4; 150 mM sodium chloride (NaCl); 1% (v/v) Octylphenyl-polyethylene glycol (IGEPAL CA-630); 0.5% (w/v) Sodium Deoxycholate (DOC); and 0.1% (w/v) Sodium Dodecyl Sulfate (SDS); 1 mM Dithiothreitol (DTT); and cOmplete Protease Inhibitor Cocktail (Roche, Basel, Switzerland) at 4°C for 10 minutes with end-over-end rotation. Lysates were then centrifuged at maximum speed in a 4°C microcentrifuge for 10 min. The supernatants were transferred to new microcentrifuge tubes and supplemented with NuPage LDS sample buffer (Invitrogen, Carlsbad, CA) and NuPage reducing agent (Invitrogen) prior to a 10 minute heat denaturation at 95°C. Lysates were resolved on a 4–12% Bis-Tris SDS-PAGE gel (Life Technologies, San Diego, CA), followed by wet transfer to PVDF membranes (Bio-Rad, Hercules, CA) for 4 hours at 85V using Towbin buffer: 25mM Tris base, pH 9.2; 192 mM Glycine; 20% (v/v) Methanol. Immunoblots were blocked with 5% (w/v) blotting grade nonfat dry milk (Apex Bioresearch Products) in TBS-T: 20 mM Tris pH 7.4; 150 mM NaCl, 0.1% Polysorbate 20 (Tween 20) for 1 hour. Primary antibodies were diluted in TBS-T supplemented with 5% (w/v) BSA and rocked overnight. Primary antibody adsorbed membranes were rinsed three times in TBS-T and subsequently incubated with the appropriate HRP-conjugated secondary antibodies. Membranes were rinsed again three times in TBS-T and developed with SuperSignal West Pico PLUS Chemiluminescent Substrate (Thermo Fisher Scientific) on a ChemiDoc MP Imaging System (Bio-Rad) using Imagelab (Bio-Rad) software. Specifications for antibodies are described in Supplementary File 6.

The ability of Cas9 Control, NINL KO, and NIN KO to respond to IFNα was assayed by first culturing cells in the presence or absence of 1000U IFNα. Eighteen hours post-treatment with IFNα the cells were harvested, lysed and immunoblotted as described above for STAT1, Phospho-STAT1 (Tyr701), STAT2, Phospho-STAT2 (Tyr690), MX1, IFIT3, OAS1, and ISG15 (Supplementary File 6).

526 **RNASeq and analysis**

527 All experiments for RNAseq were performed with three biological replicates. Total RNA from
528 mock-treated or IFNα-treated cell lines (1000 U, 24 hour treatment) was extracted using an
529 RNeasy Plus Mini Kit (Qiagen) as indicated in the manufacturer's protocol. The Illumina Stranded
530 mRNA prep kit was used to generate dual-indexed cDNA libraries and the resulting libraries were
531 sequenced on an Illumina NovaSeq 6000 instrument. Total RNA was assessed for quality using
532 an Agilent Tapestation 4200, and samples with an RNA Integrity Number (RIN) greater than 8.0
533 were used to generate RNA sequencing libraries using the TruSeq Stranded mRNA Sample Prep
534 Kit with TruSeq Unique Dual Indexes (Illumina, San Diego, CA). Samples were processed
535 following manufacturer's instructions, starting with 500 ng of RNA and modifying RNA shear time
536 to five minutes. Resulting libraries were multiplexed and sequenced with 100 basepair (bp) paired
537 end reads (PE100) to a depth of approximately 25 million reads per sample on an Illumina
538 NovaSeq 6000 instrument. Samples were demuxltiplexed using bcl2fastq v2.20 Conversion
539 Software (Illumina, San Diego, CA). Sequencing reads were quantified with Salmon (Patro et al.,
540 2017) in a quasi-mapping-based mode to the reference genome. Read quantifications were
541 imported and differentially expressed genes across experimental conditions were identified using
542 the R package DESeq2 (Love et al., 2014). Reactome pathway analysis was performed by
543 inputting the list of genes with significantly lower expression (adjusted p-value $\leq$0.05, $\log_2$-fold
544 change $\leq$-1) in NINL KO cells treated with IFNα relative to WT cells treated with IFNα into the
545 "Analyze Gene List" tool at reactome.org (Jassal et al., 2020). RNA sequencing data have been
546 deposited in GEO under accession code GSE20678
547 (https://www.ncbi.nlm.nih.gov/geo/query/acc.cgi?acc=GSE206784).
548
549 **Viral stocks**
550 CVB3 and EMCV viral stocks were generated by co-transfection of CVB3-Nancy or EMCV-Mengo
551 infectious clone plasmids with a plasmid expressing T7 RNA polymerase (generous gifts from Dr.

552 Julie Pfeiffer, UT Southwestern, see Supplementary File 5) as previously described (McCune et
553 al., 2020). The supernatant was harvested, quantified by plaque assay on Vero cells (CVB3) (see
554 below) or TCID50 on HEK293Tcells (EMCV), and frozen in aliquots at −80°C. Wild-type vaccinia
555 virus Western Reserve strain (NCBI accession NC_006998.1) (VacV WT) and the J3 cap1-
556 methlytransferase K175R vaccinia virus mutant (Latner et al., 2002) (VacV J3) were gifts from Dr.
557 Richard Condit (University of Florida). VacV was amplified in BHK cells and quantified by plaque
558 assay as described below. VSV-GFP (Indiana strain, gift from Dr. John Rose (Yale University))
559 was amplified in BSC40s and quantified by plaque assay as described below. Sindbis virus (SinV)
560 was generated by electroporation of *in vitro* transcribed RNA from plasmid SINV TE/5′2J-GFP
561 (strain Toto1101, from Dr. Charles Rice, Rockefeller University) into BHK cells as previously
562 described (Bick et al., 2003) and quantified by plaque assay on BHK cells as described below.
563
564 **Viral Infection and quantification**
565 For quantification of VSV and SinV, cells (as indicated in each experiment) were seeded in 24-
566 well plates and grown overnight, followed by the addition of 2,500 plaque forming units (PFU)/well
567 of VSV or 250,000 PFU/well SinV. Nine hours after infection for VSV or 24 hours after infection
568 for SinV, viral supernatant was harvested from infected cells. The resulting supernatant was
569 serially 10-fold diluted in 24-well plates in DMEM containing 10% FBS and overlaid on BHK cells
570 (ATCC) at 80% confluency for 1 hour. Supernatant was removed from cells 60-120 minutes post-
571 infection and cells were overlaid with complete DMEM media containing 0.8% carboxymethyl
572 cellulose (MilliporeSigma, Burlington, MA, USA). After 24 hours, the overlay was aspirated and
573 the cells were stained with 0.1% Crystal Violet in 20% ethanol, and then de-stained with 20%
574 ethanol. Viral concentrations were determined by manually counting plaques.
575 For quantification of CVB3, cells (as indicated in each experiment) were seeded in 24-well
576 plates and grown overnight, followed by the addition of 25,000 PFU/well virus. Twenty-four hours
577 after infection, viral supernatant was harvested from the infected cells, serially 10-fold diluted in

12-well plates in DMEM containing 10% FBS and overlaid on Vero cells (ATCC) at 80% confluency for 1 hour. Supernatant was removed from cells 60-120 minutes post-infection and cells were overlaid with complete DMEM media containing 1% agarose (Fisher Scientific) and 1 mg/mL neomycin (Research Products International, Mount Prospect, IL, USA) to enhance plaque visualization (Woods Acevedo et al., 2019). After 48 hours, agarose plugs were washed out with water and the cells were stained with 0.1% Crystal Violet in 20% ethanol, and then de-stained with 20% ethanol. Viral concentrations were determined by manually counting plaques.

For quantification of VacV WT and VacV J3, cells (as indicated in each experiment) were seeded in 24-well plates and grown overnight, followed by the addition of 25,000 PFU/well virus. Twenty-four hours after infection, cell-associated virus was harvested by freeze-thaw lysis of the infected cells. Following pelleting of cell debris, virus-containing supernatant was serially 10-fold diluted in 24-well plates in DMEM containing 10% FBS and overlaid on BSC40 cells (ATCC) at 80% confluency. After 48 hours, the medium was aspirated, and the cells were stained with 0.1% Crystal Violet in 20% ethanol, and then de-stained with 20% ethanol. Viral concentrations were determined by manually counting plaques.

Prediction of NINL cleavage sites by enterovirus 3C^{pro}

Putative enterovirus 3C^{pro} cleavage sites within human NINL were predicted using a previously generated polyprotein cleavage motif (Tsu et al., 2021a) constructed from >500 non-redundant enterovirus polyprotein sequences. A FIMO motif search against human NINL was conducted using a 0.002 p-value threshold, which we previously determined was sufficient to capture of 95% of enterovirus cleavage sites (Tsu et al., 2021a). To enrich for cleavage sites that may be species-specific, sites in which there is variability in the P1 or P1' sites, which are the primary determinants of cleavage specificity (Tsu et al., 2021a), are reported.

NINL protease cleavage assays

HEK293T cells were co-transfected with 100 ng of epitope-tagged human WT NINL, the NINL double mutant (Q827R, Q1032R), the NINL triple mutant (Q231R, Q827R, Q1032R), NINL isoform 2 or the NINL isoform 2 mutant (Q231R) and with 250 ng of HA-tagged protease-producing constructs for $3C^{pro}$ assays or 5 ng for $3CL^{pro}$ assays. Twenty-four hours post-transfection, the cells were harvested, lysed in 1x NuPAGE LDS sample buffer (Invitrogen) containing 5% β-mercaptoethanol (Thermo Fisher Scientific) and immunoblotted as described above.

NINL virus cleavage assays

HEK293T cells were transfected with 100 ng of epitope tagged human WT NINL, the NINL double mutant (Q827R, Q1032R), the NINL triple mutant (Q231R, Q827R, Q1032R), NINL isoform 2 or the NINL isoform 2 mutant (Q231R). At 24 h post-transfection, cells were infected with CVB3 or EMCV at a concentration of 250,000 PFU/well. Nine hours post-infection, the cells were harvested, lysed in 1x NuPAGE LDS sample buffer (Invitrogen) containing 5% β-mercaptoethanol (Thermo Fisher Scientific) and immunoblotted as described above.

Immunofluorescence

Cells were grown on fibronectin-coated acid-washed #1.5 glass coverslips. As applicable, cells underwent the desired treatment prior to a brief permeabilization with 300 μl of 0.5 % TritonX-100 (MilliporeSigma) in PHEM buffer: 60 mM piperazine-N,N′-bis(2-ethanesulfonic acid) (PIPES), 25 mM 4-(2-hydroxyethyl)-1-piperazineethanesulfonic acid (HEPES), 10 mM Ethylene glycol-bis(2-aminoethylether)-N,N,N′,N′-tetraacetic acid (EGTA), and 4 mM magnesium sulfate heptahydrate ($MgSO_4 \cdot 7H_20$). After five minutes, 100 μl of a 4% (v/v) formaldehyde (Electron Microscopy Sciences, Hatfield, PA) and 0.5% (v/v) glutaraldehyde (Electron Microscopy Sciences) in PHEM solution was added slowly to the cells and allowed to incubate. After two minutes, all buffer was

aspirated from the cells and replaced with the same 4% (v/v) formaldehyde and 0.5% (v/v) glutaraldehyde in PHEM solution and incubated for 20 minutes at 37 °C. After this incubation, the cells were washed three times for five minutes each in PHEM-T (PHEM + 0.1 % TritonX-100). The cells were then blocked for one hour with a 5% secondary-matched serum solution in PHEM supplemented with 30 mM glycine. The blocking solution was then removed and the desired primary antibodies were added and incubated overnight at 4 °C. The following day the cells were washed three times for five minutes in PHEM-T and immunostained with the appropriate secondary antibodies for one hour at room temperature. The cells were then washed with PHEM-T and counter-stained with 4′,6-diamidino-2-phenylindole (DAPI, Biotium, Fremont, CA). The cells and coverslips were mounted on glass slides with Prolong Glass Antifade Mountant (Thermo Scientific). See Supplementary File 2 for a list of all antibodies.

Confocal microscopy

Cells were imaged using a CSU-W1 spinning disk confocal scanner unit (Yokogawa Electric Corporation, Musashino, Tokyo, Japan) coupled to a six-line (405 nm, 445nm, 488 nm, 514nm, 561 nm, and 640 nm) LUN-F-XL laser engine (Nikon Instruments Incorporated, Melville, NY, USA). Emission light from the DAPI, Alexa Fluor 561, and Alexa Fluor 647 was filtered using a quad primary dichroic (405/488/568/647nm; Semrock, Rochester, NY, USA) and individual bandpass emission filters mounted within the W1 scan head for each channel (450/50, 595/50, and 700/70; Chroma Technology Corporation, Bellows Falls, VT). The W1 was mounted on a Nikon Ti2-E and an Apo TIRF 60x 1.49 NA objective was used to collect images. Image stacks were acquired using a piezo Z-insert (Mad City Labs, Madison, WI, USA). Illumination and image acquisition was controlled by NIS Elements Advanced Research software (Nikon Instruments Incorporated).

Peroxisome trafficking assay

For imaging of peroxisome accumulation at the centrosome in the presence or absence of $3C^{pro}$ or CVB3 infection, 25,000 U-2 OS cells were plated on fibronectin-coated coverslips and incubated overnight. For $3C^{pro}$ transfected experiments, cells were transfected with the PEX3-Emerald-FKBP construct and either the cleavable NINL-FRB construct or the uncleavable NINL triple mutant construct with or without co-transfection of CVB3 $3C^{pro}$. Eighteen hours after transfection, the cells were treated with or without 1 μM rapalog (Takara Bio) for one hour prior to fixation. For CVB3 infections experiments, the cells were only transfected with the PEX3-Emerald-FKBP construct and either the cleavable NINL-FRB construct or the uncleavable NINL triple mutant construct. Eighteen hours after transfection, cells were infected with 250,000 PFU (MOI ~ 2) or mock infected. Five hours later, cells were treated with or without 1 μM rapalog for one hour (for a total of six hours of infection) prior to fixation. Cells from both $3C^{pro}$ experiments and CVB3 infection experiments were fixed and immunostained as described above. Specifically, the centrosome was immunostained with anti-pericentrin rabbit polyclonal antibodies, goat anti-rabbit IgG (H + L) Alexa Fluor-647 (Thermo Fisher Scientific) and counterstained with DAPI prior to mounting. Z-stacks were acquired using a piezo Z stage. Separate image channels were acquired sequentially using bandpass filters for each channel DAPI: 455/50, PEX3-Emerald-FKBP: 525/50, pericentrin: 705/75.

Max intensity projections of Z-stacks were created in FIJI for each separate channel to quantify the peroxisome accumulation at the centrosome. The brightest pericentrin puncta in the 647 channel was identified as the centrosome, and a 60 pixel-wide circle was drawn around it to create a region of interest (ROI). A whole cell ROI was then manually drawn by adjusting the brightness/contrast module's "Maximum" slider to saturate cellular boundaries. The fluorescence intensity at the centrosome and throughout the cell was then quantified by applying each ROI to the PEX3-Emerald-FKBP/488 channel. The percentage of total fluorescence present at the centrosome was calculated by dividing the intensity of fluorescence at the centrosome by the intensity of fluorescence throughout the cell. The area of the centrosome ROI was then divided

by the area of the whole cell ROI to calculate the percentage of the cell's area that the centrosome ROI comprised. The fluorescence intensity ratio was then divided by the area ratio and plotted using GraphPad Prism. Kruskal–Wallis with Dunn's post hoc test for multiple comparisons was performed using GraphPad Prism.

Acknowledgements

We thank members of the Daugherty and Reck-Peterson laboratories, as well as Patrick Mitchell, and Alistair Russell, for helpful suggestions and comments on the manuscript. We also thank the Nikon Imaging Center at UC San Diego and Dr. Eric Griffis for advice on imaging and analysis. This work was supported by grants from the National Institutes of Health (R35 GM133633 (MDD), R35 GM141825 ((SRP), the Pew Biomedical Scholars Program (MDD), Burroughs Wellcome Fund (MDD), and the Howard Hughes Medical Institute (SRP). Individual support was provided by the National Institutes of Health (T32 GM007240 to DAS, CB, BVT, and APR), the Howard Hughes Medical Institute Gilliam Fellowship (DAS), and the National Science Foundation GRFP (DAS and CB).

Competing Interests

The authors have no competing interests to declare.

References

Agrawal R, Gillies JP, Zang JL, Zhang J, Garrott SR, Shibuya H, Nandakumar J, DeSantis ME. 2022. The KASH5 protein involved in meiotic chromosomal movements is a novel dynein activating adaptor (preprint). Cell Biology. doi:10.1101/2022.03.11.483947

Altschul SF, Gish W, Miller W, Myers EW, Lipman DJ. 1990. Basic local alignment search tool. *Journal of Molecular Biology* **215**:403–410. doi:10.1016/S0022-2836(05)80360-2

Bachmann-Gagescu R, Dona M, Hetterschijt L, Tonnaer E, Peters T, de Vrieze E, Mans DA, van Beersum SEC, Phelps IG, Arts HH, Keunen JE, Ueffing M, Roepman R, Boldt K, Doherty D, Moens CB, Neuhauss SCF, Kremer H, van Wijk E. 2015. The Ciliopathy Protein CC2D2A Associates with NINL and Functions in RAB8-MICAL3-Regulated Vesicle Trafficking. *PLoS Genet* **11**:e1005575. doi:10.1371/journal.pgen.1005575

Beachboard DC, Horner SM. 2016. Innate immune evasion strategies of DNA and RNA viruses. *Current Opinion in Microbiology* **32**:113–119. doi:10.1016/j.mib.2016.05.015

Bick MJ, Carroll J-WN, Gao G, Goff SP, Rice CM, MacDonald MR. 2003. Expression of the zinc-finger antiviral protein inhibits alphavirus replication. *J Virol* **77**:11555–11562. doi:10.1128/jvi.77.21.11555-11562.2003

Brandenburg B, Zhuang X. 2007. Virus trafficking - learning from single-virus tracking. *Nature reviews Microbiology* **5**:197–208.

Casenghi M, Meraldi P, Weinhart U, Duncan PI, Körner R, Nigg EA. 2003. Polo-like kinase 1 regulates Nlp, a centrosome protein involved in microtubule nucleation. *Developmental cell* **5**:113–125.

Cason SE, Carman PJ, Van Duyne C, Goldsmith J, Dominguez R, Holzbaur ELF. 2021. Sequential dynein effectors regulate axonal autophagosome motility in a maturation-

723 dependent pathway. *Journal of Cell Biology* **220**:e202010179.
724 doi:10.1083/jcb.202010179
725 Chaaban S, Carter AP. 2022. Structure of dynein-dynactin on microtubules shows tandem
726 recruitment of cargo adaptors (preprint). Molecular Biology.
727 doi:10.1101/2022.03.17.482250
728 Chen Y, Li C, Wang N, Wu Z, Zhang J, Yan J, Wei Y, Peng Q, Qi J. 2022. Identification of
729 LINC00654-NINL Regulatory Axis in Diffuse Large B-Cell Lymphoma In Silico
730 Analysis. *Front Oncol* **12**:883301. doi:10.3389/fonc.2022.883301
731 Daffis S, Szretter KJ, Schriewer J, Li J, Youn S, Errett J, Lin T-Y, Schneller S, Zust R, Dong H,
732 Thiel V, Sen GC, Fensterl V, Klimstra WB, Pierson TC, Buller RM, Gale Jr M, Shi P-Y,
733 Diamond MS. 2010. 2′-O methylation of the viral mRNA cap evades host restriction by
734 IFIT family members. *Nature* **468**:452–456. doi:10.1038/nature09489
735 Daugherty MD, Malik HS. 2012. Rules of Engagement: Molecular Insights from Host-Virus
736 Arms Races. *Annual Review of Genetics* **46**:677–700. doi:10.1146/annurev-genet-
737 110711-155522
738 Daugherty MD, Schaller AM, Geballe AP, Malik HS. 2016. Evolution-guided functional
739 analyses reveal diverse antiviral specificities encoded by IFIT1 genes in mammals. *eLife*
740 **5**:e14228. doi:10.7554/eLife.14228
741 Dodding MP, Way M. 2011. Coupling viruses to dynein and kinesin-1. *The EMBO journal*
742 **30**:3527–3539.
743 Döhner K, Nagel C-H, Sodeik B. 2005. Viral stop-and-go along microtubules: taking a ride with
744 dynein and kinesins. *Trends in microbiology* **13**:320–327.

745 Dona M, Bachmann-Gagescu R, Texier Y, Toedt G, Hetterschijt L, Tonnaer EL, Peters TA, van
746 Beersum SEC, Bergboer JGM, Horn N, de Vrieze E, Slijkerman RWN, van Reeuwijk J,
747 Flik G, Keunen JE, Ueffing M, Gibson TJ, Roepman R, Boldt K, Kremer H, van Wijk E.
748 2015. NINL and DZANK1 Co-function in Vesicle Transport and Are Essential for
749 Photoreceptor Development in Zebrafish. *PLoS genetics* **11**:e1005574.
750 Duggal NK, Emerman M. 2012. Evolutionary conflicts between viruses and restriction factors
751 shape immunity. *Nat Rev Immunol* **12**:687–695. doi:10.1038/nri3295
752 Enard D, Cai L, Gwennap C, Petrov DA. 2016. Viruses are a dominant driver of protein
753 adaptation in mammals. *Elife* **5**. doi:10.7554/eLife.12469
754 Enard D, Petrov DA. 2018. Evidence that RNA Viruses Drove Adaptive Introgression between
755 Neanderthals and Modern Humans. *Cell* **175**:360-371.e13. doi:10.1016/j.cell.2018.08.034
756 Fenton AR, Jongens TA, Holzbaur ELF. 2021. Mitochondrial adaptor TRAK2 activates and
757 functionally links opposing kinesin and dynein motors. *Nat Commun* **12**:4578.
758 doi:10.1038/s41467-021-24862-7
759 Gordon DE, Jang GM, Bouhaddou M, Xu J, Obernier K, White KM, O'Meara MJ, Rezelj VV,
760 Guo JZ, Swaney DL, Tummino TA, Hüttenhain R, Kaake RM, Richards AL,
761 Tutuncuoglu B, Foussard H, Batra J, Haas K, Modak M, Kim M, Haas P, Polacco BJ,
762 Braberg H, Fabius JM, Eckhardt M, Soucheray M, Bennett MJ, Cakir M, McGregor MJ,
763 Li Q, Meyer B, Roesch F, Vallet T, Mac Kain A, Miorin L, Moreno E, Naing ZZC, Zhou
764 Y, Peng S, Shi Y, Zhang Z, Shen W, Kirby IT, Melnyk JE, Chorba JS, Lou K, Dai SA,
765 Barrio-Hernandez I, Memon D, Hernandez-Armenta C, Lyu J, Mathy CJP, Perica T, Pilla
766 KB, Ganesan SJ, Saltzberg DJ, Rakesh R, Liu X, Rosenthal SB, Calviello L,
767 Venkataramanan S, Liboy-Lugo J, Lin Y, Huang X-P, Liu Y, Wankowicz SA, Bohn M,

768 Safari M, Ugur FS, Koh C, Savar NS, Tran QD, Shengjuler D, Fletcher SJ, O'Neal MC,
769 Cai Y, Chang JCJ, Broadhurst DJ, Klippsten S, Sharp PP, Wenzell NA, Kuzuoglu-Ozturk
770 D, Wang H-Y, Trenker R, Young JM, Cavero DA, Hiatt J, Roth TL, Rathore U,
771 Subramanian A, Noack J, Hubert M, Stroud RM, Frankel AD, Rosenberg OS, Verba KA,
772 Agard DA, Ott M, Emerman M, Jura N, von Zastrow M, Verdin E, Ashworth A,
773 Schwartz O, d'Enfert C, Mukherjee S, Jacobson M, Malik HS, Fujimori DG, Ideker T,
774 Craik CS, Floor SN, Fraser JS, Gross JD, Sali A, Roth BL, Ruggero D, Taunton J,
775 Kortemme T, Beltrao P, Vignuzzi M, García-Sastre A, Shokat KM, Shoichet BK, Krogan
776 NJ. 2020. A SARS-CoV-2 protein interaction map reveals targets for drug repurposing.
777 *Nature* **583**:459–468. doi:10.1038/s41586-020-2286-9

778 Ho SN, Biggar SR, Spencer DM, Schreiber SL, Crabtree GR. 1996. Dimeric ligands define a
779 role for transcriptional activation domains in reinitiation. *Nature* **382**:822–826.
780 doi:10.1038/382822a0

781 Hoffmann H-H, Schneider WM, Rice CM. 2015. Interferons and viruses: an evolutionary arms
782 race of molecular interactions. *Trends Immunol* **36**:124–138. doi:10.1016/j.it.2015.01.004

783 Htet ZM, Gillies JP, Baker RW, Leschziner AE, DeSantis ME, Reck-Peterson SL. 2020. LIS1
784 promotes the formation of activated cytoplasmic dynein-1 complexes. *Nat Cell Biol*
785 **22**:518–525. doi:10.1038/s41556-020-0506-z

786 Huynh W, Vale RD. 2017. Disease-associated mutations in human BICD2 hyperactivate motility
787 of dynein–dynactin. *Journal of Cell Biology* **216**:3051–3060. doi:10.1083/jcb.201703201

788 Ilan-Ber T, Ilan Y. 2019. The role of microtubules in the immune system and as potential targets
789 for gut-based immunotherapy. *Molecular Immunology* **111**:73–82.
790 doi:10.1016/j.molimm.2019.04.014

Jassal B, Matthews L, Viteri G, Gong C, Lorente P, Fabregat A, Sidiropoulos K, Cook J, Gillespie M, Haw R, Loney F, May B, Milacic M, Rothfels K, Sevilla C, Shamovsky V, Shorser S, Varusai T, Weiser J, Wu G, Stein L, Hermjakob H, D'Eustachio P. 2020. The reactome pathway knowledgebase. *Nucleic Acids Res* **48**:D498–D503. doi:10.1093/nar/gkz1031

Johnson B, VanBlargan LA, Xu W, White JP, Shan C, Shi P-Y, Zhang R, Adhikari J, Gross ML, Leung DW, Diamond MS, Amarasinghe GK. 2018. Human IFIT3 Modulates IFIT1 RNA Binding Specificity and Protein Stability. *Immunity* **48**:487-499.e5. doi:10.1016/j.immuni.2018.01.014

Kapitein LC, Schlager MA, van der Zwan WA, Wulf PS, Keijzer N, Hoogenraad CC. 2010. Probing Intracellular Motor Protein Activity Using an Inducible Cargo Trafficking Assay. *Biophysical Journal* **99**:2143–2152. doi:10.1016/j.bpj.2010.07.055

Kast DJ, Dominguez R. 2017. The Cytoskeleton–Autophagy Connection. *Current Biology* **27**:R318–R326. doi:10.1016/j.cub.2017.02.061

Katoh K. 2002. MAFFT: a novel method for rapid multiple sequence alignment based on fast Fourier transform. *Nucleic Acids Research* **30**:3059–3066. doi:10.1093/nar/gkf436

Kersten FF, van Wijk E, Hetterschijt L, Bauβ K, Peters TA, Aslanyan MG, van der Zwaag B, Wolfrum U, Keunen JE, Roepman R, Kremer H. 2012. The mitotic spindle protein SPAG5/Astrin connects to the Usher protein network postmitotically. *Cilia* **1**:2.

Kosakovsky Pond SL, Frost SDW. 2005. Not So Different After All: A Comparison of Methods for Detecting Amino Acid Sites Under Selection. *Molecular Biology and Evolution* **22**:1208–1222. doi:10.1093/molbev/msi105

Labun K, Montague TG, Gagnon JA, Thyme SB, Valen E. 2016. CHOPCHOP v2: a web tool for the next generation of CRISPR genome engineering. *Nucleic Acids Res* **44**:W272-276. doi:10.1093/nar/gkw398

Latner DR, Thompson JM, Gershon PD, Storrs C, Condit RC. 2002. The positive transcription elongation factor activity of the vaccinia virus J3 protein is independent from its (nucleoside-2'-O-) methyltransferase and poly(A) polymerase stimulatory functions. *Virology* **301**:64–80. doi:10.1006/viro.2002.1538

Lau CK, O'Reilly FJ, Santhanam B, Lacey SE, Rappsilber J, Carter AP. 2021. Cryo-EM reveals the complex architecture of dynactin's shoulder region and pointed end. *EMBO J* **40**:e106164. doi:10.15252/embj.2020106164

Lee I-G, Cason SE, Alqassim SS, Holzbaur ELF, Dominguez R. 2020. A tunable LIC1-adaptor interaction modulates dynein activity in a cargo-specific manner. *Nat Commun* **11**:5695. doi:10.1038/s41467-020-19538-7

Lei J, Hilgenfeld R. 2017. RNA-virus proteases counteracting host innate immunity. *FEBS Lett* **591**:3190–3210. doi:10.1002/1873-3468.12827

Liu Y, Salter HK, Holding AN, Johnson CM, Stephens E, Lukavsky PJ, Walshaw J, Bullock SL. 2013. Bicaudal-D uses a parallel, homodimeric coiled coil with heterotypic registry to coordinate recruitment of cargos to dynein. *Genes Dev* **27**:1233–1246. doi:10.1101/gad.212381.112

Love MI, Huber W, Anders S. 2014. Moderated estimation of fold change and dispersion for RNA-seq data with DESeq2. *Genome Biol* **15**:550. doi:10.1186/s13059-014-0550-8

Luby-Phelps K. 2000. Cytoarchitecture and physical properties of cytoplasm: volume, viscosity, diffusion, intracellular surface area. *International review of cytology* **192**:189–221.

836 Man SM, Kanneganti T-D. 2016. Converging roles of caspases in inflammasome activation, cell
837 death and innate immunity. *Nat Rev Immunol* **16**:7–21. doi:10.1038/nri.2015.7
838 McCune BT, Lanahan MR, tenOever BR, Pfeiffer JK. 2020. Rapid Dissemination and
839 Monopolization of Viral Populations in Mice Revealed Using a Panel of Barcoded
840 Viruses. *J Virol* **94**:e01590-19. doi:10.1128/JVI.01590-19
841 McKenney RJ, Huynh W, Tanenbaum ME, Bhabha G, Vale RD. 2014. Activation of
842 cytoplasmic dynein motility by dynactin-cargo adapter complexes. *Science (New York,*
843 *NY)* **345**:337–341.
844 Meyerson NR, Sawyer SL. 2011. Two-stepping through time: mammals and viruses. *Trends in*
845 *Microbiology* **19**:286–294. doi:10.1016/j.tim.2011.03.006
846 Mostowy S, Shenoy AR. 2015. The cytoskeleton in cell-autonomous immunity: structural
847 determinants of host defence. *Nat Rev Immunol* **15**:559–573. doi:10.1038/nri3877
848 Murrell B, Wertheim JO, Moola S, Weighill T, Scheffler K, Kosakovsky Pond SL. 2012.
849 Detecting Individual Sites Subject to Episodic Diversifying Selection. *PLoS Genet*
850 **8**:e1002764. doi:10.1371/journal.pgen.1002764
851 Ng CS, Stobart CC, Luo H. 2021. Innate immune evasion mediated by picornaviral 3C protease:
852 Possible lessons for coronaviral 3C-like protease? *Rev Med Virol* **31**:1–22.
853 doi:10.1002/rmv.2206
854 Olenick MA, Holzbaur ELF. 2019. Dynein activators and adaptors at a glance. *J Cell Sci* **132**.
855 doi:10.1242/jcs.227132
856 Passmore JB, Nijenhuis W, Kapitein LC. 2021. From observing to controlling: Inducible control
857 of organelle dynamics and interactions. *Current Opinion in Cell Biology* **71**:69–76.
858 doi:10.1016/j.ceb.2021.02.002

Patro R, Duggal G, Love MI, Irizarry RA, Kingsford C. 2017. Salmon provides fast and bias-aware quantification of transcript expression. *Nat Methods* **14**:417–419. doi:10.1038/nmeth.4197

Radtke K, Döhner K, Sodeik B. 2006. Viral interactions with the cytoskeleton: a hitchhiker's guide to the cell. *Cellular Microbiology* **8**:387–400.

Reck-Peterson SL, Redwine WB, Vale RD, Carter AP. 2018. The cytoplasmic dynein transport machinery and its many cargoes. *Nature Reviews Molecular Cell Biology* **19**:382–398. doi:10.1038/s41580-018-0004-3

Redwine WB, DeSantis ME, Hollyer I, Htet ZM, Tran PT, Swanson SK, Florens L, Washburn MP, Reck-Peterson SL. 2017. The human cytoplasmic dynein interactome reveals novel activators of motility. *eLife* **6**:379.

Rothenburg S, Brennan G. 2020. Species-Specific Host–Virus Interactions: Implications for Viral Host Range and Virulence. *Trends in Microbiology* **28**:46–56. doi:10.1016/j.tim.2019.08.007

Schlager MA, Hoang HT, Urnavicius L, Bullock SL, Carter AP. 2014. In vitro reconstitution of a highly processive recombinant human dynein complex. *The EMBO journal* **33**:1855–1868.

Schoggins JW. 2019. Interferon-Stimulated Genes: What Do They All Do? *Annu Rev Virol* **6**:567–584. doi:10.1146/annurev-virology-092818-015756

Seksek O, Biwersi J, Verkman AS. 1997. Translational Diffusion of Macromolecule-sized Solutes in Cytoplasm and Nucleus. *Journal of Cell Biology* **138**:131–142. doi:10.1083/jcb.138.1.131

881 Tenthorey JL, Emerman M, Malik HS. 2022. Evolutionary Landscapes of Host-Virus Arms
882 Races. *Annu Rev Immunol* **40**:271–294. doi:10.1146/annurev-immunol-072621-084422
883 Terawaki S, Yoshikane A, Higuchi Y, Wakamatsu K. 2015. Structural basis for cargo binding
884 and autoinhibition of Bicaudal-D1 by a parallel coiled-coil with homotypic registry.
885 *Biochemical and Biophysical Research Communications* **460**:451–456.
886 doi:10.1016/j.bbrc.2015.03.054
887 Tsu B, Beierschmitt C, Ryan AP, Agarwal R, Mitchell PS, Daugherty MD. 2021a. Diverse viral
888 proteases activate the NLRP1 inflammasome. *eLife* **10**:e60609. doi:10.7554/eLife.60609
889 Tsu B, Fay EJ, Nguyen KT, Corley MR, Hosuru B, Dominguez VA, Daugherty MD. 2021b.
890 Running With Scissors: Evolutionary Conflicts Between Viral Proteases and the Host
891 Immune System. *Front Immunol* **12**:769543. doi:10.3389/fimmu.2021.769543
892 Urnavicius L, Zhang K, Diamant AG, Motz C, Schlager MA, Yu M, Patel NA, Robinson CV,
893 Carter AP. 2015. The structure of the dynactin complex and its interaction with dynein.
894 *Science (New York, NY)* **347**:1441–1446.
895 van Wijk E, Kersten FFJ, Kartono A, Mans DA, Brandwijk K, Letteboer SJF, Peters TA, Märker
896 T, Yan X, Cremers CWRJ, Cremers FPM, Wolfrum U, Roepman R, Kremer H. 2009.
897 Usher syndrome and Leber congenital amaurosis are molecularly linked via a novel
898 isoform of the centrosomal ninein-like protein. *Human molecular genetics* **18**:51–64.
899 Wang Y, Huynh W, Skokan TD, Lu W, Weiss A, Vale RD. 2019. CRACR2a is a calcium-
900 activated dynein adaptor protein that regulates endocytic traffic. *Journal of Cell Biology*
901 **218**:1619–1633. doi:10.1083/jcb.201806097

902 Weaver S, Shank SD, Spielman SJ, Li M, Muse SV, Kosakovsky Pond SL. 2018. Datamonkey
903 2.0: A Modern Web Application for Characterizing Selective and Other Evolutionary
904 Processes. *Molecular Biology and Evolution* **35**:773–777. doi:10.1093/molbev/msx335
905 Woods Acevedo MA, Erickson AK, Pfeiffer JK. 2019. The Antibiotic Neomycin Enhances
906 Coxsackievirus Plaque Formation. *mSphere* **4**:e00632-18. doi:10.1128/mSphere.00632-
907 18
908 Xiao W, Yeerken D, Li J, Li Z, Jiang L, Li D, Fu M, Ma L, Song Y, Zhang W, Zhan Q. 2021.
909 Nlp promotes autophagy through facilitating the interaction of Rab7 and FYCO1. *Signal*
910 *Transduct Target Ther* **6**:152. doi:10.1038/s41392-021-00543-1
911 Yang Z. 2007. PAML 4: Phylogenetic Analysis by Maximum Likelihood. *Molecular Biology*
912 *and Evolution* **24**:1586–1591. doi:10.1093/molbev/msm088
913 Yu H, Bruneau RC, Brennan G, Rothenburg S. 2021. Battle Royale: Innate Recognition of
914 Poxviruses and Viral Immune Evasion. *Biomedicines* **9**:765.
915 doi:10.3390/biomedicines9070765
916

917 **Figure Legends**

918

919 **Figure 1. The dynein activating adaptor, NINL, has evolved under positive selection in**
920 **primates.** (**A**) A schematic of the cytoplasmic dynein-1 transport machinery, which includes
921 dynein and dynactin subunits (blue) and an activating adaptor (orange). Dynein moves toward
922 the minus end of microtubules (blue arrow). (**B**) A scatterplot displaying evolutionary signatures
923 of selection for 23 dynein and dynactin genes (blue) and 13 dynein activating adaptor genes
924 (orange). The x-axis displays the rate of non-synonymous changes (dN) divided by the rate of
925 synonymous changes (dS) in the coding sequence across primate evolution. The y-axis displays

926 the calculated probability of the gene having evolved under positive selection using PAML.
927 Complete data are found in Figure 1–figure supplement 1. (**C**) A schematic of human NINL isoform
928 1 with EF hand (dark grey) and coiled-coil (light grey) domains shown. The amino-terminal
929 dynein/dynactin binding region and the carboxy-terminal candidate cargo binding domains are
930 indicated. Sites of positive selection predicted by three evolutionary models are shown as colored
931 arrows: PAML (light red), FEL (blue), MEME (orange). A full list of sites and their calculated
932 probabilities are shown in Figure 1–figure supplement 2. (**D**) Full-length NINL, the dynein/dynactin
933 binding amino-terminus of NINL and the candidate cargo binding carboxy-terminus of NINL were
934 analyzed for signatures of positive selection. Select dN/dS and p-values are shown, with
935 additional evolutionary data in Figure 1–figure supplement 3.
936
937 **Figure 2. The antiviral potency of IFNα is reduced in NINL KO cells.** (**A**) Immunoblots of WT
938 A549 cells, and CRISPR/Cas9-generated NINL and NIN KO A549 cells probed with the indicated
939 antibodies. GAPDH served as a loading control. Protein molecular weight markers are shown in
940 kilodaltons (kDa) to the left of each immunoblot. Representative images from three biological
941 replicates are shown. (**B**) WT, NINL KO, and NIN KO A549 cells were treated with 100U IFNα for
942 24 hours and then infected with VSV (5000 PFU/mL, MOI ≈ 0.01). Virus-containing supernatants
943 were collected nine hours post-infection and viral titers (y-axis, plaque forming units per mL) were
944 determined by plaque assay. (**C**) WT or NINL KO U-2 OS cells were treated with 100U IFNα for
945 24 hours and then infected with VSV (5000 PFU/mL, MOI ≈ 0.01). Virus-containing supernatant
946 was collected nine hours post-infection and viral titers (y-axis, plaque forming units per mL) were
947 determined by plaque assay. (**D**) WT or NINL KO A549 cells were treated with 100U IFNα for 24
948 hours and then infected with Sindbis virus (500,000 PFU/mL, MOI ≈ 1.0) (left) or treated with
949 1000U IFNα for 24 hours and then infected with coxsackievirus B3 (5000 PFU/mL, MOI ≈ 0.01)
950 (right). Virus-containing supernatants were collected 24 hours post-infection and viral titers (y-

951 axis, plaque forming units per mL) were determined by plaque assay. (**B-D**) Data are presented
952 as mean ± standard deviation of three biological replicates, with individual points shown. Data
953 were analyzed by two-way ANOVA with Tukey's method adjustment for multiple comparisons for
954 IFNα treatment within each cell line, two-way ANOVA interaction comparison for IFNα interaction
955 between cell lines. *p<0.05, **p<0.01, ***p<0.001, ****p<0.0001, ns = not significant.
956
957 **Figure 2–figure supplement 1. Validation of CRISPR/Cas9-editing to generate NINL and NIN**
958 **KO cells.** (**A**) Confocal micrographs displayed as maximum intensity projections of WT and NINL
959 KO A549 cells. Immunostaining with anti-pericentrin and anti-tubulin antibodies was used to
960 visualize centrosomes and microtubules, respectively. Nuclei were visualized with DAPI. 15 μm
961 scale bars are shown in the merged micrographs. Dashed white lines denote cellular
962 boundaries. Representative micrographs from two biological replicates are shown. (**B**) Sequence
963 verification of exon 2-targeted NINL KO A549 cells. An excerpt of the WT *NINL* sequence is
964 shown with the CRISPR-targeting sgRNA and PAM sequences indicated (top), the sequencing
965 chromatogram (middle), and the sequence of the NINL KO (bottom). (**C**) Sequence verification of
966 exon 5-targeted NIN KO A549 cells. (**D**) Immunoblots of control (CTRL) HCT116 and U-2 OS
967 cells, and CRISPR/Cas9-generated NINL and NIN KO HCT116 and U-2 OS cells probed with the
968 indicated antibodies. GAPDH served as a loading control. Protein molecular weight markers are
969 shown in kilodaltons (kDa) to the left of each immunoblot. Representative images from three
970 biological replicates are shown. (**E**) Sequence verification of exon 2-targeted NINL KO U-2 OS
971 cells. (**F**) Sequence verification of exon 6-targeted NINL KO HCT116 cells. (**G**) Sequence
972 verification of exon 3-targeted NIN KO HCT116 cells.
973
974 **Figure 2–figure supplement 2. Reduction of IFNα-mediated antiviral response is observed**
975 **across multiple cell lines.** (**A**) A549 WT, NINL KO, or NIN KO cells were treated with 100U IFNα
976 for 24 hours, then infected with Sindbis virus (500,000 PFU/mL, MOI ≈ 1.0). Cells were collected

977 24 hours post-infection and viral titers (y-axis, plaque forming units per mL) were determined by
978 plaque assay. WT and NINL KO data are reproduced from Figure 2D for comparison. (**B**) U-2 OS
979 WT or NINL KO cells were treated, infected, harvested, and quantified as described in **(A).** (**C**)
980 A549 WT, NINL KO, or NIN KO cells were treated with 1000U IFNα for 24 hours, then infected
981 with coxsackievirus B3 (5,000 PFU/mL, MOI ≈ 0.01). Cells were collected 24 hours post-infection
982 and viral titers (y-axis, plaque forming units per mL) were determined by plaque assay. WT and
983 NINL KO data are reproduced from Figure 2D for comparison. (**D**) U-2 OS WT or NINL KO cells
984 treated, infected, harvested, and quantified as described in (C). (A-D) Data are presented as
985 mean ± standard deviation of three biological replicates, with individual points shown. Data were
986 analyzed by two-way ANOVA with Tukey's method adjustment for multiple comparisons for IFNα
987 treatment within each cell line, two-way ANOVA interaction comparison for IFNα interaction
988 between cell lines. *p<0.05, **p<0.01, ***p<0.001, ****p<0.0001, ns = not significant.
989
990 **Figure 3. NINL KO cells fail to mount an effective IFN response.** (**A**) Immunoblot of extracts
991 from WT, NINL KO, and NIN KO A549 cells untreated (-) or treated (+) with IFNα. Immunoblots
992 were probed with anti-STAT2, anti-Phospho-STAT2 (Tyr690), anti-STAT1, anti-Phospho-STAT1
993 (Tyr701), anti-Mx1, anti-IFIT3, anti-OAS1, anti-ISG15, and anti-β-actin antibodies. Predicted
994 protein molecular weights are shown in kilodaltons (kDa) to the left of each immunoblot.
995 Representative images from three biological replicates are shown. (**B**) Differential ISG expression
996 in WT, NINL KO, and NIN KO cells induced with IFNα. ISGs were identified as the 88 genes
997 whose expression was upregulated in WT cells after IFNα pretreatment (Figure 3-figure
998 supplement 2). Experiments were performed with three biological replicates. Data are displayed
999 as a violin plot of ISG expression in NIN KO or NINL KO cells relative to WT cells. **** = p<0.0001
1000 based on paired t-test. Dotted line indicates mean. Individual data points for ISGs shown in panel
1001 (A) are indicated. (**C**) A549 WT cells were treated with 1000U IFNα for 24 hours, then infected
1002 with wild-type vaccinia virus (WT VacV) or J3 mutant vaccinia virus (J3 VacV) (50,000 PFU/mL,

MOI ≈ 0.1). Cell-associated virus was collected 24 hours post-infection and viral titers (y-axis, plaque forming units per mL) were determined by plaque assay. (**D**) A549 NINL KO cells were treated, infected, harvested, and quantified as described in (C). (C-D) Data are presented as mean ± standard deviation of three biological replicates, with individual points shown. Data were analyzed by two-way ANOVA with Tukey's method adjustment for multiple comparisons for IFNα treatment within each cell line, two-way ANOVA interaction comparison for IFNα interaction between cell lines. ****p<0.0001, ns = not significant.

Figure 3–figure supplement 1. Reduced ISG production occurs following NINL KO in multiple cell lines generated using different CRISPR gRNAs Immunoblot of extracts from WT, NINL KO, NIN KO HCT116 cells and WT and NINL KO U-2 OS cells untreated or treated with IFNα. Immunoblots were probed with anti-STAT2, anti-Phospho-STAT2 (Tyr690), anti-STAT1, anti-Phospho-STAT1 (Tyr701), anti-Mx1, anti-IFIT3, anti-OAS1, anti-ISG15, and anti-β-actin antibodies. Predicted protein molecular weights are shown in kilodaltons (kDa) to the left of each immunoblot. Representative images from three biological replicates are shown.

Figure 3–figure supplement 2. Identification of 88 ISGs in WT A549 cells. Differential gene expression from RNAseq analyses of WT A549 cells pretreated with IFNα compared to untreated. Each condition (untreated or IFNα) was performed with three biological replicates, with independent RNA extractions, sequencing library preparation, and sequencing. RNA levels for a total of 14102 genes (grey dots) could be compared (see Materials and Methods and Supplementary File 4). Only 88 genes (red dots) showed a statistically significant upregulation (adjusted p-value ≤0.05, $\log_2$-fold change ≥1), which we refer to in subsequent analyses as ISGs.

Figure 3–figure supplement 3. Interferon induction has a reduced effect on ISG expression in NINL KO cells. Differential gene expression of 88 ISGs (identified in Figure 3–figure

supplement 2**)** from RNAseq analyses of the indicated cell lines pretreated with IFNα compared to untreated. Each condition (untreated or IFNα) was performed with three biological replicates, with independent RNA extractions, sequencing library preparation, and sequencing. Only the 88 genes significantly upregulated in WT cells, which we refer to as ISGs (adjusted p-value ≤0.05, log_2-fold change ≥1), are shown for each cell line. Data are displayed as a violin plot of ISG upregulation, with the dotted line indicating the mean. ****p<0.0001 based on one-way ANOVA test.

Figure 3–figure supplement 4. Differential gene expression in NINL KO and NIN KO cells compared to WT cells. (**A**) Differential gene expression from RNAseq analyses of NINL KO cells treated with IFNα compared to WT A549 cells treated with IFNα. Each cell line (NINL KO or WT) was treated with IFNα with three biological replicates, with independent RNA extractions, sequencing library preparation, and sequencing. RNA levels for a total of 18563 genes (grey dots) could be compared (see Materials and Methods and Supplementary File 4). Orange dots highlight the 72 ISGs that are significantly differentially expressed between cell lines, with the majority (66 of 72) of ISGs significantly lower in NINL KO cells (adjusted p-value ≤0.05, log_2-fold change ≤-1). (**B**) Differential gene expression from RNAseq analyses of NIN KO cells treated with IFNα compared to WT A549 cells treated with IFNα. RNA levels for a total of 15794 genes (grey dots) could be compared (see Materials and Methods and Supplementary File 4). Dark grey dots highlight the 11 ISGs that are significantly differentially expressed between cell lines. (**C**) Reactome pathway analysis (Jassal et al., 2020) of the 3549 genes with significantly lower expression (adjusted p-value ≤0.05, log_2-fold change ≤-1) in NINL KO cells treated with IFNα relative to WT cells treated with IFNα. Only the two pathways shown were identified as significantly different between the cell lines. The number of genes found to be lower in NINL KO cells (# entities found) compared to the number of genes in the indicated pathway (# entities total) is shown. The p-value, as well as false discovery rate (FDR) adjusted p-values are shown.

Figure 3–figure supplement 5. NINL KO results in loss of interferon sensitivity of the VacV J3 mutant.

(**A**) A549 NIN KO cells were treated with 1000U IFNα for 24 hours, then infected with wildtype vaccinia virus (VacV WT) or J3 mutant vaccinia virus (J3 VacV) (50,000 PFU/mL, MOI ≈ 0.1). Cell-associated virus was collected 24 hours post-infection and viral titers (y-axis, plaque forming units per mL) were determined by plaque assay. (**B**) U-2 OS WT cells were treated with 1000U IFNα for 24 hours, then infected with wild-type vaccinia virus or J3 mutant vaccinia virus (50,000 PFU/mL, MOI ≈ 0.1). Cells were collected 24 hours post-infection and viral titers (y-axis, plaque forming units per mL) were determined by plaque assay. (**C**) U-2 OS NINL KO cells were treated, infected, harvested, and collected as indicated in (B). (A-C) Data are presented as mean ± standard deviation of three biological replicates, with individual points shown. Data were analyzed by two-way ANOVA with Tukey's method adjustment for multiple comparisons for IFNα treatment within each viral infection, two-way ANOVA interaction comparison for IFNα interaction between viral infections. **p<0.01, *** p<0.001, ns = not significant.

Figure 4. NINL is cleaved at species-specific sites by virally encoded proteases. (**A**) Schematic of human NINL, with positions of predicted $3C^{pro}$ cleavage sites annotated. Shown are the four amino acids on each side of the predicted cleavage site in human NINL, along with the residue positions and cleavage score predicted using a motif search with the consensus enterovirus cleavage site (see Methods). (**B**) NINL sequences from 12 primate species and mice for each predicted $3C^{pro}$ cleavage site. Amino acid changes relative to human NINL are highlighted in colors to denote differences in polarity and charge. (**C**) Schematic of 3xFLAG-NINL-Myc isoform 1 and isoform 2 constructs, with predicted molecular weights for both amino-terminal (FLAG) and carboxy-terminal (Myc) products upon cleavage by $3C^{pro}$. (**D**) Immunoblots of extracts from HEK293T cells co-transfected with the indicated NINL constructs and either CVB3 $3C^{pro}$ or

the catalytically inactive (C147A) CVB3 3C^{pro} (mutant). Immunoblots were probed with anti-FLAG (NINL amino-terminus), anti-Myc (NINL carboxy-terminus), anti-HA (3C^{pro}), and anti-GAPDH (loading control). Arrows to the left of each immunoblot indicate full-length products as well as products corresponding to cleavage at the indicated amino acid residue. Protein molecular weight markers are shown in kilodaltons (kDa) to the right of each immunoblot. Representative images from three biological replicates are shown. (**E**) Immunoblots of extracts from HEK293T cells transfected with the indicated amino-terminal FLAG and carboxyl-terminal Myc tagged NINL constructs and infected with either CVB3 or EMCV (500,000 PFU/mL, MOI ≈ 1.0 for 8 h). Immunoblots were probed with anti-FLAG (NINL amino-terminus), anti-Myc (NINL carboxy-terminus), and anti-GAPDH (loading control). Arrows to the left of each immunoblot indicate full length products as well as products corresponding to CVB3 3C^{pro} cleavage at the indicated amino acid residue. Protein molecular weight markers are shown in kilodaltons (kDa) to the right of each immunoblot. Representative images from three biological replicates are shown.

Figure 4–figure supplement 1. **3C and 3CL proteases from diverse viruses cleave NINL at redundant and unique sites.** (**A**) Immunoblots of extracts from HEK293T cells co-transfected with the indicated NINL constructs and 3C^{pro} from the indicated picornavirus. CVB3: coxsackievirus B3, CVB3 mutant: catalytically inactive (C147A) CVB3 3C^{pro}, EV71: enterovirus A71, PV1: poliovirus 1, EV68: enterovirus D68, HRVA: human rhinovirus A, EMCV: encephalomyocarditis virus, Parecho: parechovirus A, HepA: hepatitis A virus, Sali: salivirus A. Immunoblots were probed with anti-Myc (NINL carboxy-terminus), anti-HA (3C^{pro}), and anti-GAPDH (loading control). Arrows to the left of each immunoblot indicate full-length products as well as products corresponding to CVB3 3C^{pro} cleavage at the indicated amino acid residue. Protein molecular weight markers are shown in kilodaltons (kDa) to the right of each immunoblot. Representative images from three biological replicates are shown. (**B**) Immunoblots of extracts from HEK293T cells co-transfected with the indicated NINL constructs and the indicated

coronaviral 3CL^{pro}. SARS2: SARS-CoV-2, SARS2 mutant: catalytically inactive (C145A) SARS-CoV-2 3CL^{pro} SARS1: SARS-CoV, NL63: HCoV-NL63. 3CL^{pros} were expressed as self-cleaving constructs that remove a carboxy-terminal mCherry-HA tag. Immunoblots were probed with anti-Myc (NINL carboxy-terminal), anti-HA (cleaved mCherry-HA from catalytically active protease constructs, or eGFP-3CL^{pro}-mCherry-HA from catalytically inactive protease constructs), and anti-GAPDH (loading control). Arrows to the left of each immunoblot indicate full-length products as well as products corresponding to SARS-CoV-2 3CL^{pro} cleavage at the indicated amino acid residue. Protein molecular weight markers are shown in kilodaltons (kDa) to the right of each immunoblot. Representative images from three biological replicates are shown.

Figure 5. CVB3 3C^{pro} cleavage of NINL prevents rapalog-induced dynein-dependent transport of intracellular cargoes. (**A**) Schematic of the peroxisomal trafficking assay. The peroxisomal targeting signal (PTS1) of human PEX3 (amino acids 1–42) was fused to mEmerald and FKBP and a truncated NINL (amino acids 1-1062) was fused to FRB. Dynein-dependent accumulation of peroxisomes at the centrosome, where most minus-ends are located, is initiated by the rapalog-mediated heterodimerization of FKBP and FRB. Blue arrow indicates dynein motility. (**B**) Indicated FRB and FKBP constructs transiently expressed with (+) or without (-) the transient co-expression of HA-tagged CVB3 3C^{pro} in HEK293T cells. Immunoblots were probed with anti-FLAG, anti-FKBP, anti-GAPDH and anti-HA antibodies. Protein molecular weight markers are shown in kilodaltons (kDa) to the left of each immunoblot. Representative images from three biological replicates are shown. (**C**) Confocal micrographs are displayed as maximum intensity projections of U-2 OS cells, transfected with Pex3-mEmerald-FKBP and the indicated cleavable or uncleavable NINL-FRB fusion constructs with or without the co-expression of CVB3 3C^{pro}. Where indicated, cells were treated for one hour with ethanol (EtOH) as a control or 1 μM rapalog in EtOH prior to fixation. Centrosomes were immunostained with anti-pericentrin and nuclei were visualized with DAPI. 15 μm scale bars indicated in lower left corner of merged

micrographs. Yellow rectangles denote region of cropped inset. Dashed white lines denote cellular boundaries. Representative micrographs from three biological replicates are shown. (**D**) Schematic of the analysis pipeline. (**E**) Quantification of peroxisomal trafficking assays from three biological replicates. The fluorescence intensity of Pex3-mEmerald-FKBP at the centrosome was normalized to the whole-cell fluorescence, and to the areas of the regions of interest used to quantify centrosome versus whole-cell fluorescence. Each datapoint corresponds to an individual cell. The dark grey, large, outlined circles correspond to the mean for each biological replicate. For each condition n = ~80. The mean across all replicates is denoted by the bold line. Data were analyzed using Kruskal–Wallis with Dunn's post hoc test for multiple comparisons. ****p<0.0001, ns = not significant.

Figure 5–figure supplement 1. Peroxisome distribution remains consistent regardless of presence of CVB3 3C^{pro} prior to rapalog induced dynein-dependent transport. (**A**) Schematic of NINL-FRB fusion constructs. Predicted molecular weights for each 3xFLAG tagged amino-terminal cleavage product produced by 3C^{pro}. (**B**) Peroxisome distribution controls. Confocal micrographs displayed as maximum intensity projections of U-2 OS cells, transfected with Pex3-mEmerald-FKBP and the indicated cleavable or uncleavable NINL-FRB fusion constructs with or without the co-expression of CVB3 3C^{pro} treated for one hour with ethanol (EtOH) prior to fixation. Centrosomes were immunostained with anti-pericentrin and nuclei were visualized with DAPI. 15 μm scale bars are indicated in the lower left corner of the merged micrographs. Yellow rectangles denote region of cropped inset. Dashed white lines denote cellular boundaries. Representative micrographs from three biological replicates are shown. (**C**) Quantification of peroxisomal trafficking assay from three biological replicates. The fluorescence intensity of Pex3-mEmerald-FKBP at the centrosome was normalized to the whole-cell fluorescence, and to the areas of the regions of interest used to quantify centrosome versus whole-cell fluorescence. Each datapoint corresponds to an individual cell and biological replicates

can be distinguished by shade. For each condition n = ~80. The mean across all replicates is denoted by the bold line. Bold circles correspond to the mean for each biological replicate. Data were analyzed using Kruskal–Wallis with Dunn's post hoc test for multiple comparisons. ns = not significant.

Figure 6. Cleavage of NINL during viral infection prevents dynein-dependent transport of an intracellular cargo. (**A**) Confocal micrographs displayed as maximum intensity projections of uninfected or CVB3 infected U-2 OS cells. Cells were transfected with Pex3-mEmerald-FKBP and the indicated cleavable or uncleavable NINL-FRB fusion constructs, and infected (or mock infected) with CVB3 (500,000 PFU/ml, MOI = ~2) for five hours. Cells were then treated for one hour with ethanol (EtOH) or 1 μM rapalog prior to fixation. Centrosomes were immunostained with anti-pericentrin and nuclei were visualized with DAPI. 15 μm scale bars are indicated in the lower left corner of the merged micrographs. Yellow rectangles denote region of cropped inset. Dashed white lines denote cellular boundaries. Representative micrographs from three biological replicates are shown. (**B**) Quantification of peroxisomal trafficking assays from three biological replicates. The fluorescence intensity of Pex3-mEmerald-FKBP at the centrosome was normalized to the whole-cell fluorescence, and to the areas of the regions of interest used to quantify centrosome versus whole-cell fluorescence. Each datapoint corresponds to an individual cell and biological replicates can be distinguished by shade. For each condition n = ~80. The mean across all replicates is denoted by the bold line. Bold circles correspond to the mean for each biological replicate. Data were analyzed using Kruskal–Wallis with Dunn's post hoc test for multiple comparisons. ****p<0.0001, ns = not significant. (**C**) Schematic of the rapalog-induced pericentrosomal accumulation of peroxisomes and loss of accumulation upon viral infection.

Figure 6–figure supplement 1. Peroxisome distribution remains consistent regardless of CVB3 infection prior to rapalog induced dynein-mediated transport. (**A**) Peroxisome

distribution controls. Confocal micrographs displayed as maximum intensity projections of uninfected or CVB3 infected U-2 OS cells expressing Pex3-mEmerald-FKBP and the indicated cleavable or uncleavable NINL-FRB fusion constructs treated for one hour with ethanol (EtOH) prior to fixation. Centrosomes were immunostained with anti-pericentrin and nuclei were stained with DAPI. 15 μm scale bars are indicated in the lower left corner of the merged micrographs. Yellow rectangles denote region of cropped inset. Dashed white lines denote cellular boundaries. Representative micrographs from three biological replicates are shown. (**B**) Quantification of peroxisomal trafficking assays from three biological replicates. Fluorescence intensity of Pex3-mEmerald-FKBP at the centrosome was normalized to the whole-cell fluorescence, and to the areas of the regions of interest used to quantify centrosome versus whole-cell fluorescence. Each datapoint corresponds to an individual cell and biological replicates can be distinguished by shade. For each condition n = ~80. The mean across all replicates is denoted by a bold line. Bold circles correspond to the mean for each biological replicate. Data were analyzed using Kruskal–Wallis with Dunn's post hoc test for multiple comparisons. ns = not significant.

Supplementary Files

Supplementary File 1. Evolutionary analyses on dynein, dynactin, and activating adapter genes. Statistics from PAML analyses on individual dynein, dynactin, and activating adapter genes.

Supplementary File 2. Codon positions in NINL predicted to be evolving under positive selection. NINL codon positions and probability scores from PAML, FEL, and MEME analyses.

Supplementary File 3. Evolutionary analysis of N-terminal and C-terminal domains of NINL. Statistics from PAML analyses on NINL full length, N-terminal domain only, and C-terminal domain only.

Supplementary File 4. Differentially regulated transcripts in WT A549, NINL KO, and NIN KO cell lines induced and uninduced with IFN. Results from DEseq comparison from RNAseq of indicated cell lines and under different induction conditions.

Supplementary File 5. List of primers and gBlocks used. Spreadsheet that details the generation or sourcing of all plasmids used throughout this study.

Supplementary File 6. List of antibodies used for immunoblots and immunofluorescence. Spreadsheet that details each antibody name, manufacturer, catalog number, and dilutions used.

Figure 2-source data 1. Full raw unedited images for Figure 2A.

Figure 2-source data 2. Individual data values for Figure 2B- D.

Figure 2-Figure supplement 1-source data 1. Full raw unedited images for Figure 2-Figure supplement 1D.

Figure 2-Figure supplement 2-source data 1. Individual data values for Figure 2-Figure supplement 2A-D.

Figure 3-source data 1. Full raw unedited images for Figure 3A.

Figure 3-source data 2. Individual data values for Figure 3C.

Figure 3-Figure supplement 1-source data 1. Full raw unedited images for Figure 3-Figure supplement 1.

Figure 3-Figure supplement 5-source data 1. Individual data values for Figure 3-Figure supplement 5A-C.

Figure 4-source data 1. Full raw unedited images for Figure 4D-E.

Figure 4-Figure supplement 1-source data 1. Full raw unedited images for Figure 4-Figure supplement 1A-B.

Figure 5-source data 1. Full raw unedited images for Figure 5B.

Figure 5-source data 2. Individual data values for Figure 5E and Figure 5-Figure supplement 1C.

Figure 6-source data 1. Individual data values for Figure 6B and Figure 6-Figure supplement 1B.